

DFT study of itinerant ferromagnetism in p -doped monolayers of MoS₂

Yuqiang Gao,^{1,2,*} Nirmal Ganguli,^{1,†} and Paul J. Kelly^{1,3,‡}

¹*Faculty of Science and Technology and MESA⁺ Institute for Nanotechnology,
University of Twente, P.O. Box 217, 7500 AE Enschede, The Netherlands*

²*Department of Applied Physics, Northwestern Polytechnical University, Xi'an, China*

³*The Center for Advanced Quantum Studies and Department of Physics,
Beijing Normal University, 100875 Beijing, China*

(Dated: 25 October 2019)

We use density functional theory to explore the possibility of making the semiconducting transition-metal dichalcogenide MoS₂ ferromagnetic by introducing holes into the narrow Mo d band that forms the top of the valence band. In the single impurity limit, the repulsive Coulomb potential of an acceptor atom and intervalley scattering lead to a twofold orbitally degenerate effective-mass like e' state being formed from Mo $d_{x^2-y^2}$ and d_{xy} states, bound to the K and K' valence band maxima. It also leads to a singly degenerate a'_1 state with Mo $d_{3z^2-r^2}$ character bound to the slightly lower lying valence band maximum at Γ . Within the accuracy of our calculations, these e' and a'_1 states are degenerate for MoS₂ and accommodate the hole that polarizes fully in the local spin density approximation in the impurity limit. With spin-orbit coupling included, we find a single ion magnetic anisotropy of ~ 5 meV favouring out-of-plane orientation of the magnetic moment. Pairs of such hole states introduced by V, Nb or Ta doping are found to couple ferromagnetically unless the dopant atoms are too close in which case the magnetic moments are quenched by the formation of spin singlets. Combining these exchange interactions with Monte Carlo calculations allows us to estimate ordering temperatures as a function of x . For $x \sim 9\%$, Curie temperatures as high as 100K for Nb and Ta and in excess of 160K for V doping are predicted. Factors limiting the ordering temperature are identified and suggestions made to circumvent these limitations.

PACS numbers: 75.70.Ak, 73.22.-f, 75.30.Hx, 75.50.Pp

I. INTRODUCTION

The discovery of ferromagnetism in (In,Mn)As¹ and (Ga,Mn)As² and predictions for achieving room temperature ordering³ sparked a huge effort to realize a dilute magnetic semiconductor (DMS) that might lead to a semiconductor-based spin electronics (“Spintronics”). After twenty-five years of intensive research, the maximum ordering temperature has stagnated at values too low for extensive applications.⁴ The number of material systems being considered has proliferated but it is not clear what the fundamental limit is to the ordering temperature achievable in any particular material system. There are many reasons for the low ordering temperatures^{5,6} but the essential dilemma is that the open d shell states of magnetic impurities like Mn are quite localized. While this favours the onsite exchange interaction that is the origin of the Hund’s-rule spin alignment and makes the ionic moment insensitive to temperature, it leads to weaker exchange interactions between pairs of impurity ions that determine the Curie temperature T_C , the ferromagnetic ordering temperature. To increase T_C , the concentration of impurity atoms has to be increased. This is accompanied by a variety of adverse effects such as a nonuniform distribution of magnetic impurities or the formation of antisite defects that are electron donors which counter the intended increase in the concentration of holes. In many semiconductors, transition metal ions introduce “deep levels”, tightly bound partially occupied states in the fundamental gap of the semiconductor. At high dopant concentrations, these form deep

impurity bands that dominate the (transport) properties of a material that is no longer a semiconductor and from the electronic structure point of view, is an entirely new material.

In a quite different context, it was long believed that long-range magnetic ordering would not be possible in two-dimensional (2D) materials.^{7,8} However the observation of ferromagnetism in ultrathin epitaxial layers of e.g., Fe on Au substrates demonstrated that the Mermin-Wagner theorem is not watertight, violation of the proof usually being attributed to magnetocrystalline anisotropy.⁹ The recent observation of ferromagnetic ordering in two different chromium-based 2D crystalline materials Cr₂Ge₂Te₆¹⁰ and CrI₃¹¹ nonetheless attracted considerable attention.¹² One reason was because of the general interest in 2D materials, triggered by spectacular observations on graphene.^{13–15} This interest was reinforced by the realization that the properties of semiconductors like MoS₂ could also be importantly different in few- and mono-layer form^{16–18} and was compounded by the desirability of stacking layers of 2D materials with different properties¹⁹ whereby the lack of a ferromagnetic material in a vast profusion of 2D materials was a striking lacuna.²⁰ Because the Curie temperatures of monolayers of the chromium based materials^{10,11} is low, $\lesssim 50$ K, the very recent reports that the transition metal dichalcogenide VS₂²¹ and Fe₃GeTe₂²² exhibit ferromagnetism at room temperature acquires huge significance.

The ferromagnetism of VS₂ and VSe₂ was predicted with the aid of density functional theory (DFT) calculations.²³ The driving force behind the magnetic or-

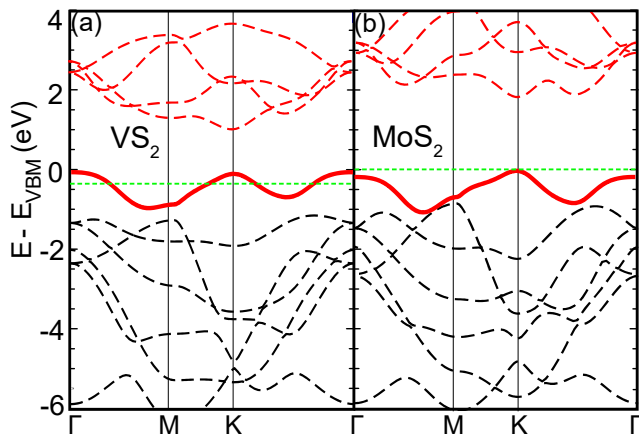


FIG. 1. Non spin-polarized band structures of monolayers of trigonal prismatic 1H VS_2 (a) and MoS_2 (b). The Fermi level is indicated by a horizontal dashed green line. The valence band maximum (VBM) at the K and K' points has mixed $d_{x^2-y^2}$ and d_{xy} character. The slightly lower-lying valence band maximum at the Γ point has $d_{3z^2-r^2}$ character.

dering can be understood in terms of the band structure of the nonmagnetic 1H phase shown in Fig. 1(a) that is very similar to that of the isostructural MoS_2 shown in Fig. 1(b) but with one valence electron per formula unit less so that it is metallic with the Fermi level situated in the middle of the solid red band. Bulk multilayered MoS_2 is a non-magnetic semiconductor with an indirect bandgap of about 1 eV. In monolayer form it was predicted to have a larger, direct gap²⁴ and this was confirmed experimentally where direct gaps of ~ 1.8 eV have been reported.^{16,17} In the figure, the “nominal” Mo $4d$ bands are indicated in red, the black bands are sulphur-derived $3p$ bands. The interaction of the Mo- d and S- p states is such that a large covalent bonding-antibonding gap is formed leaving a single Mo- d band (solid red line) with mixed $\{d_{x^2-y^2}, d_{xy}, d_{3z^2-r^2}\}$ character in the fundamental band gap.^{25,26} For MoX_2 , this band is completely filled but for VX_2 it is only half full. The dispersion of only about 1 eV leads to a high average density of states of ~ 2 states/eV and the gain in energy achieved by exchange-splitting this narrow band more than offsets the kinetic energy cost. The bandwidth reduction in 2D that leads to larger band gaps is favourable for itinerant ferromagnetism because of the higher average densities of states (DoS) than in three dimensions. Likewise $3d$ elements are more favourable than $4d$ and $4d$ more favourable than $5d$ because of the greater localization of the d electrons and concomitant smaller bandwidth as the principal quantum number decreases.

A number of intrinsic defects have been found to form local moments^{27–31} in MX_2 materials and suggestions have been made to make the MX_2 materials magnetic by adsorption of impurity atoms,^{27,28,32,33} or by substituting M or X atoms with impurity atoms.^{28,33–51} Even though the Mermin-Wagner theorem^{7,8} tells us that

there is no long range ordering in two dimensions for isotropic Heisenberg exchange, few attempts have been made to determine the exchange coupling between magnetic impurities^{33,37,38,40,41,47,51} and it was only very recently that the magnetic anisotropy of a defect was calculated, for an antisite defect in MoS_2 .³¹ Replacing some of the M atoms with Hund’s-rule coupled transition metal atoms like Mn or Fe gives rise to deep impurity levels in the semiconductor gap. Where attempts have been made to estimate the Curie temperature, the predicted values are either very low or the concentration of transition metal dopant is so high that the doped material is no longer a semiconductor.^{35,37,38,40,41,50} Based upon the electronic structure shown in Fig. 1(b), we explore a different approach to making MoS_2 ferromagnetic in this manuscript.⁵²

Group VIB Mo has a $4d^55s^1$ electronic configuration and, in a dichalcogenide like MoS_2 , is nominally Mo^{4+} with one up-spin and one down-spin d electron so it is nonmagnetic as seen in Fig. 1(b). When a Mo atom is substituted by a group VB atom like V, Nb or Ta, then the dopant atom e.g. V^{4+} , has a single unpaired d electron and a single hole is thereby introduced into the narrow Mo $4d$ band; substitution of a group IVB atom (Ti, Zr, Hf) will introduce two holes per dopant atom. In the impurity limit, the asymptotic Coulomb potential leads to a series of hydrogenic states bound to the top of the valence band; to the maxima at the K and K' points with mixed Mo $d_{x^2-y^2}$ and d_{xy} character and to the slightly lower valence band maximum at the Γ point with Mo $d_{3z^2-r^2}$ character and a large effective mass.⁵³

The aim of this paper⁵² is to determine if there are dopant atoms whose potential is sufficiently similar to that of the host Mo atom that only weakly bound, effective-mass like states are formed above the valence band edge, Fig. 2. At low concentrations these bound states should polarize and form impurity bands that have such a high density of states that they remain exchange split.⁵⁴ At finite temperatures these polarized bound holes will be excited into the valence band giving rise

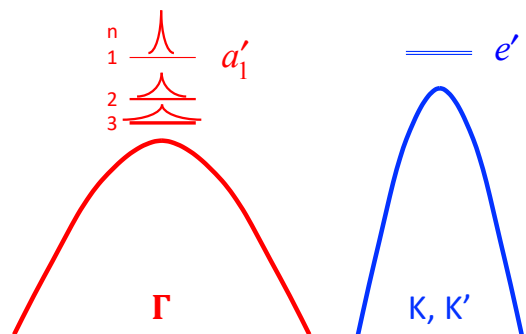


FIG. 2. Schematic of the effective mass acceptor states bound to the valence band maxima (VBM): an e' state bound to the K- K' VBM and an a'_1 state to the Γ VBM. n is the principal quantum number and only $n = 1, 2, 3$ levels of the Rydberg series are sketched at the Γ point.

to a DMS. The key objectives of this paper are to determine (i) whether single acceptor dopant atoms give rise to polarized effective-mass like states in the MoS₂ host system and to determine the position of these states with respect to the valence band edge; (ii) whether the interaction between pairs of dopant atoms favours ferromagnetic or antiferromagnetic alignment and to identify the nature of the interaction, Zener *p-d* type, double exchange etc.^{5,6} and understand the factors determining it; (iii) the magnetic anisotropy of single impurities, the so-called single ion anisotropy (SIA); (iv) the ordering temperature and express it in terms of parameterized models that describe the dopant-induced states and their interactions in order to identify the most promising regions of parameter space to realize a room temperature DMS.

To do this we use density functional theory total energy calculations to determine ground state energies of single acceptor impurities. We outline the methods used and give some technical details specific to the present work in Sec. II. Our results are presented in Sec. III beginning with a study of the single impurity limit of a substitutional vanadium atom in Sec. III A including the effects of spin polarization and local atomic relaxation. The binding of pairs of V dopants is considered in Sec. III B and their magnetic “exchange” interaction in Sec. III C with special attention being devoted to understanding the quenching of the magnetic moments of close pairs of impurity ions. In Sec. III D we briefly compare V with Nb and Ta. Sec. IV is concerned with the question of magnetic ordering and begins with a study of the single ion anisotropy of V impurities in Sec. IV A to justify using an Ising spin model with the exchange interactions from Sec. III C and the Monte Carlo techniques described in Sec. IV B to estimate ordering temperatures in Sec. IV C. A comparison of our findings with other calculations in Sec. V leads us to consider how using the generalized gradient approximation (GGA) would alter our local density approximation (LDA) results. After a brief discussion in Sec. VI some conclusions are drawn in Sec. VII.

II. COMPUTATIONAL DETAILS

Calculations of the total energy and structural optimizations were carried out within the framework of density functional theory (DFT) using the projector augmented wave (PAW) method⁵⁵ and a plane-wave basis set with a cut-off energy of 400 eV as implemented in the VASP code.^{56–58} Monolayers of MX₂ periodically repeated in the *c* direction were separated by more than 20 Å of vacuum to avoid spurious interaction.

The equilibrium structural parameters for bulk and monolayer MoS₂ were calculated in both the LDA⁶¹ and GGA⁶² and are given in Table I. It can be seen that the GGA slightly overestimates lattice constants and bond lengths compared to experiment.⁵⁹ The LDA underestimates them by more than the GGA overestimates them, a result found for many materials. In the present case, the agreement with experiment is still very reasonable

TABLE I. In-plane lattice constant *a*, distance between sulphur atoms *d*_{SS} (thickness of an MoS₂ monolayer), Mo-S bond length *d*_{MoS}, energy gap $\Delta\varepsilon_g$, and energy difference between the valence band maxima (VBM) at the K and Γ points $\Delta_{K\Gamma} = \varepsilon_K - \varepsilon_\Gamma$ in LDA and GGA for bulk and monolayer (ML) MoS₂. A van der Waals functional should be used to obtain a reasonable interlayer separation for bulk layered MoS₂. Because we are only interested in monolayers of MoS₂ in this paper, we have used the experimental value of *c* to obtain the bulk results shown here.

		<i>a</i> (Å)	<i>d</i> _{SS} (Å)	<i>d</i> _{MoS} (Å)	$\Delta\varepsilon_g$ (eV)	$\Delta_{K\Gamma}$
Bulk	GGA	3.183	3.127	2.42	0.885	-0.640
	LDA	3.125	3.115	2.38	0.748	-0.640
	Exp	3.160 ^a	3.172 ^a	2.41 ^a	1.290 ^c	-0.600 ^b
ML	GGA	3.185	3.130	2.42	1.650	0.012
	LDA	3.120	3.115	2.38	1.860	0.150
	Exp	3.160	3.172	2.41	1.900 ^c	0.140 ^b

^aRef.59, ^bRef.60 ^cRef.17

for both LDA and GGA. However, we see that for an MoS₂ monolayer the LDA gives a better description of the energy levels near the valence band maximum (VBM) than does the GGA, in particular the important quantity $\Delta_{K\Gamma} = \varepsilon_K - \varepsilon_\Gamma$, the position of the VBM at the Γ point, ε_Γ , relative to the top of the valence band at the

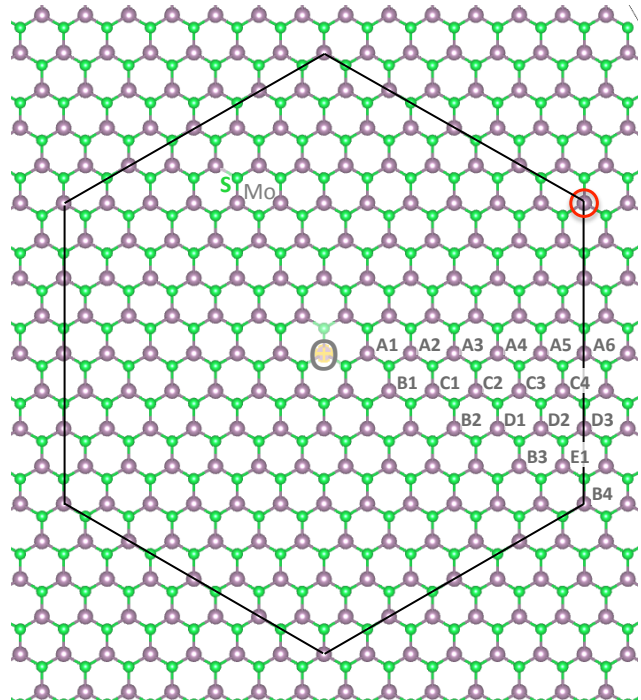


FIG. 3. Sketch of a 12×12 MoS₂ supercell with a substitutional atom at the origin, O. Shown is the more symmetric Wigner-Seitz cell. The potential on the Mo atom indicated with a red circle that is furthest from this atom will be used to identify the host valence band maximum (VBM). Mo atoms at various distances from the central atom are labelled A1-A6, B1-B4, C1-C4, D1-D3 and E1 for later reference.

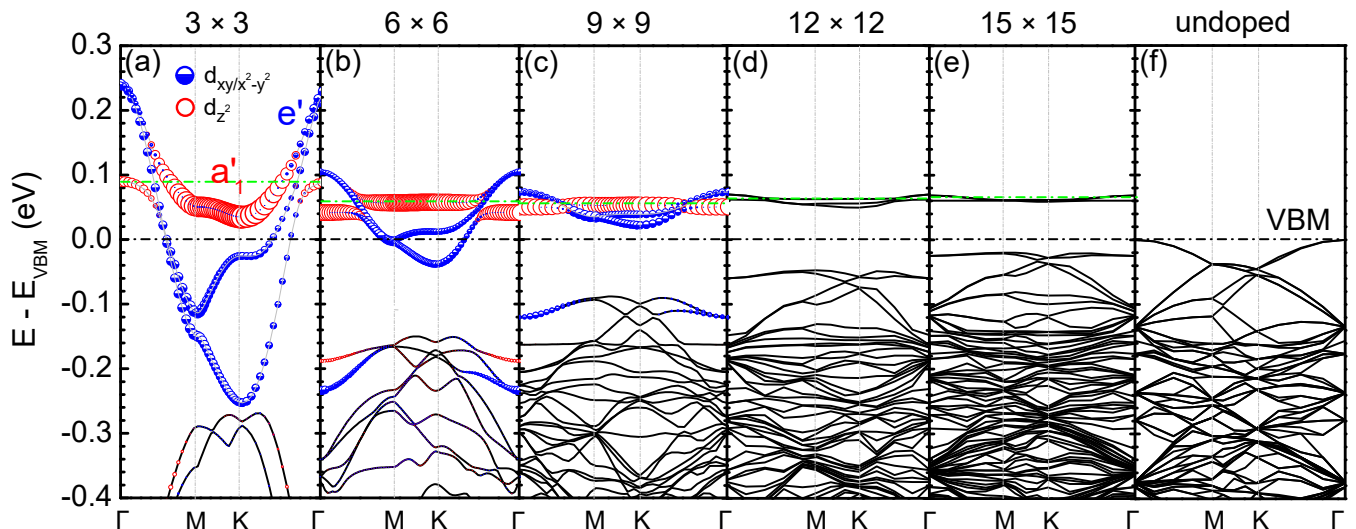


FIG. 4. The band structure of an MoS₂ monolayer with a single Mo atom replaced by V without relaxation in 3×3, 6×6, 9×9, 12×12 and 15×15 supercells (a-e) aligned with respect to the valence band maximum determined with respect to semicore level states on the Mo atom furthest from the origin (horizontal black dot-dashed line at energy zero) and of an undoped MoS₂ monolayer (f). The Fermi energy is indicated by the horizontal green dot-dashed line. The contribution from vanadium $d_{3z^2-r^2}$ and $\{d_{x^2-y^2}, d_{xy}\}$ orbitals are shown as open red circles and half-filled blue circles, respectively in (a-c) where the symbol size is proportional to the population of the corresponding state.

K point, ε_K .⁶⁰ To describe acceptor states accurately, it is important to have a good description of the host band structure in the vicinity of the VBM so we will describe exchange and correlation effects in this paper using the local spin density approximation LSDA as parameterized by Perdew and Zunger.⁶¹ Results obtained with the GGA are considered in Sec. V.

We model substitutional impurities and impurity pairs in $N \times N$ in-plane supercells with N as large as 15 using the calculated equilibrium lattice constant for the pure monolayer (ML) host, Fig. 3. Local geometries are first relaxed using $N = 6$ and only a small differential relaxation needs to be performed in the larger supercells. Interactions between pairs of impurities were studied in 12×12 supercells. The atomic positions were relaxed using a $2 \times 2 \times 1$ Γ -centered k -point mesh until the forces on each ion were smaller than 0.01 eV/Å. Spin-polarized calculations were performed with a denser mesh corresponding to 4×4 k -points for a 12×12 unit cell.

III. RESULTS

Impurity states in semiconductors are usually described in one of two limits: (i) in effective mass theory (EMT) where the main emphasis is on the Rydberg series of bound states tied to the conduction band minima or valence band maxima formed in response to a Coulomb potential or (ii) in the tight-binding limit where the main emphasis is on the local chemical binding, atomic relaxation and impurity states formed deep in the fundamental bandgap associated with an impurity potential very dif-

ferent to the host atomic potential.^{63–65} Because there is no consensus of how best to combine both aspects,⁶⁶ we consider the behaviour of shallow acceptor states in a periodic supercell geometry in some detail in the following section.

A. Single impurity limit: V in MoS₂

We begin by replacing a single Mo atom in an $N \times N$ MoS₂ supercell with a V atom with one valence electron less, Fig. 3. To more easily identify the downfolded host bands we choose N to be a multiple of three whereby the K and K' points fold down to the Γ point of the reduced BZ. The energy bands for this supercell before relaxing the local geometry are shown in Fig. 4 for $N = 3, 6, 9, 12$ and 15. The repulsive (for electrons; attractive for holes) impurity potential is seen to push not one but three impurity states out of the valence band to form localized states labeled a'_1 and e' under the local D_{3h} symmetry, Fig. 2. By projecting the corresponding wavefunctions at the Γ point onto spherical harmonics on the V_{Mo} site, we find that the singly degenerate a'_1 state has V $d_{3z^2-r^2}$ character while the e' state that is doubly degenerate at the center of the BZ has V $\{d_{x^2-y^2}, d_{xy}\}$ character. The corresponding partial charge density plots are shown on the left- respectively right-hand sides (lhs, rhs) of Fig. 5. By fitting the wave functions of the impurity states to a hydrogenic wave function $\psi(r) = A \exp(-r/a_0^*)$, we find effective Bohr radii a_0^* of 4.2 Å and 8.0 Å for the a'_1 and e' states, respectively in Fig. 5(c) and Fig. 5(d).

We identify these a'_1 and e' states with the most tightly

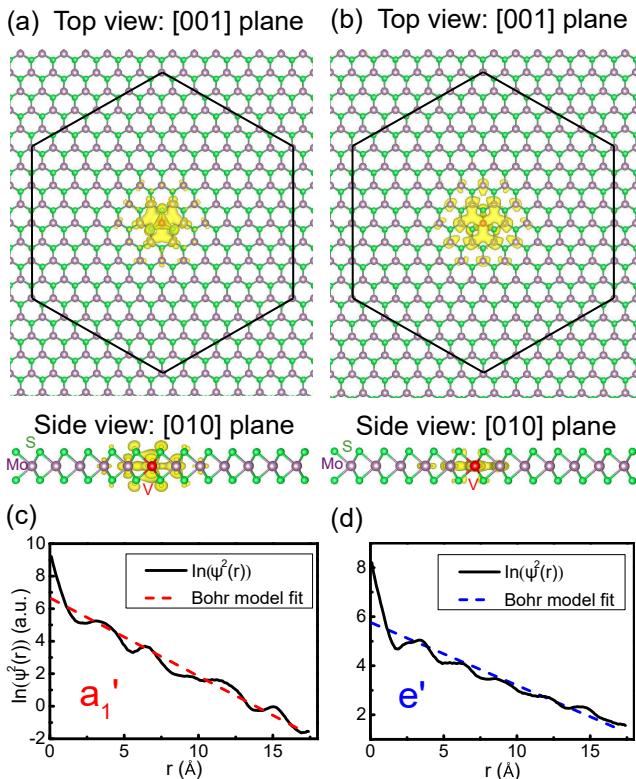


FIG. 5. Charge density plots for the a_1' (lhs) and e' (rhs) states at the Γ point in Fig. 4(d) in the central [001] plane through the Mo atoms (top view) and [010] plane (side view) for a 12×12 supercell. The isosurface levels are $0.001 e/\text{\AA}^3$. (c) and (d): circularly averaged charge densities fitted with a Bohr model.

bound (effective mass like) acceptor states formed when a screened Coulomb potential is introduced by substitution of a Mo atom by V (Nb or Ta). In the single impurity limit, intervalley scattering leads to a twofold orbitally degenerate effective mass like state formed from Mo $\{d_{x^2-y^2}, d_{xy}\}$ states bound to the K and K' valence band maxima in Fig. 1 and a singly degenerate state with Mo $d_{3z^2-r^2}$ character bound to the slightly lower lying valence band maximum at Γ in Fig. 1. Within the accuracy of our calculations, these e' and a_1' states are (accidentally) degenerate for MoS₂ and accommodate the hole that we will see polarizes fully in the local spin density approximation.⁶⁷ The shape of the dispersion of the impurity states is essentially independent of the supercell size so the bands can be described with a single effective hopping parameter. The a_1' state exhibits very little dispersion consistent with the out-of-plane $d_{3z^2-r^2}$ orbital character at Γ where the weak dispersion of the host MoS₂ bands is described by a large effective mass.⁶⁸ In the language of effective mass theory (EMT), the binding energy of the a_1' state is dominated by the central cell correction.⁶³

In the rightmost panel of Fig. 4, we show the band structure of an undoped monolayer calculated in a 15×15

supercell so the K point VBM is downfolded onto Γ . If we compare this with the impurity supercell bands on the left, we see that even for $N = 15$, Fig. 4(e), the interaction of the impurity bands and the VBM still suppresses the VBM quite noticeably, by more than 20 meV.

1. Screened impurity potential

Identifying the valence band maximum (VBM) in an impurity supercell calculation is complicated by the Rydberg series of effective mass like states associated with the single impurity whose wavefunctions will overlap with their periodic images and form bands that overlap and hybridize with the “true” valence band states, Fig. 2. To disentangle those effects, we first determine the position of the VBM with respect to Mo 4s semicore states, $\varepsilon_{4s}^{\text{Mo}}$, for an undoped monolayer of MoS₂; ε denotes a Kohn-Sham eigenvalue. For a sufficiently large impurity super-

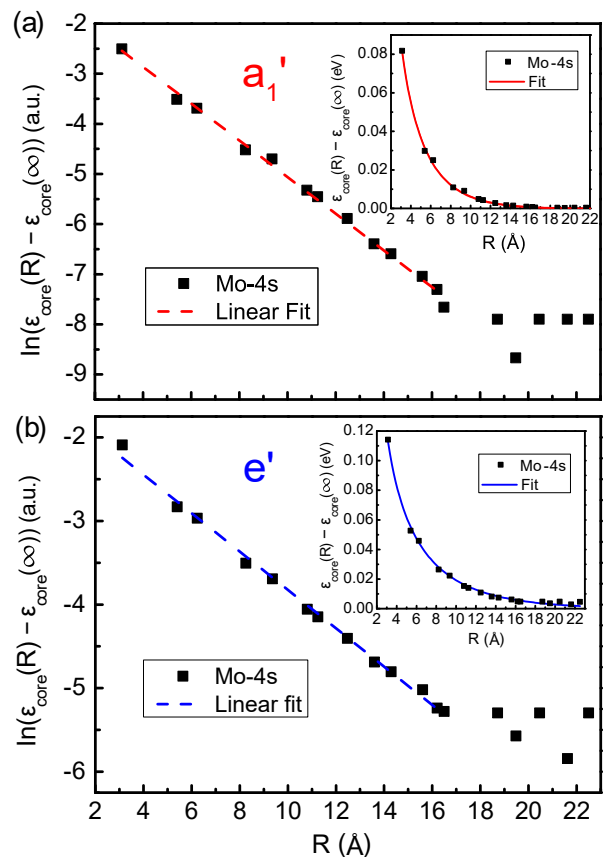


FIG. 6. Dependence of the Mo 4s semicore level on the separation from the V_{Mo} dopant ion. The Coulomb potential of the V dopant is screened by the host valence electrons and by the a_1' hole (upper panel) respectively by the e' hole (lower panel). The 18 data points refer to the 18 inequivalent Mo atoms labelled in Fig. 3. The asymptotic value $\varepsilon_{\text{core}}(\infty)$ was determined by fitting the calculated data points in the insets to an exponential wave function and using this fit (red and blue curves) to extrapolate to $R = \infty$.

cell, the position of $\varepsilon_{4s}^{\text{Mo}}$ for the Mo atom furthest from the impurity (indicated with a red circle in Fig. 3) relative to the VBM should be asymptotically equal to the corresponding energy separation for an undoped monolayer of MoS₂ because the impurity potential far from the dopant center will be completely screened by the bound charge of the neutral impurity in an a'_1 or e' bound state. To test this hypothesis quantitatively, we plot $\varepsilon_{4s}^{\text{Mo}}$ with respect to its asymptotic value as a function of the separation of Mo from the impurity V ion in the insets of Fig. 6 for $N = 12$ supercells (symbols). The corresponding results for the S semicore $2s$ state $\varepsilon_{2p}^{\text{S}}$ are shown in Appendix A and yield similar conclusions.

In an impurity supercell calculation, a localized electron in a (semi)core level on a Mo atom a distance R from the impurity atom will see a screened $1/\epsilon_r R$ repulsive potential that is partially compensated by the charge of the bound hole, $n_{\text{hole}}(r)$. Here ϵ_r is the relative static dielectric constant. We can “measure” this screened Coulomb potential by studying how Mo (and S) semicore levels behave as a function of their separation from the central V atom. The perturbing electrostatic potential seen by the core electrons has the form

$$\varepsilon_{\text{core}}(R) - \varepsilon_{\text{core}}(\infty) = \frac{1}{\epsilon_r R} \left(1 - \int_0^R n_{\text{hole}}(r) 2\pi r dr \right) \quad (1a)$$

$$= \frac{e^{-\frac{2R}{a_0^*}} \left(\frac{2R}{a_0^*} + 1 \right)}{\epsilon_r R} \quad (1b)$$

where in (1a) $n_{\text{hole}}(r) = \int_{-\infty}^{\infty} n_{\text{hole}}(r, z) dz$ and $n_{\text{hole}}(r, z)$ is obtained by integrating $|\psi_i(r, \theta, z)|^2$ over θ for $i = a'_1$ or e' . In (1b), we assume that $\psi_i(r, \theta, z)$ is the solution of a strictly two dimensional hydrogenic problem.⁶⁹ If we take the natural logarithm of (1b), the slope is $-2/a_0^*$ for large values of R and we can extract a_0^* from Fig. 6.

In the supercell band structures shown in Fig. 4, the a'_1 and e' derived states overlap and $n_{\text{hole}}(r)$ is a mixture of these two states with different masses m_h . To circumvent this complication, we calculate the electronic structure at the K (or M) point where the lowest unoccupied state has a'_1 character. By using a sufficiently small temperature broadening we can obtain the corresponding charge density and obtain the result shown in Fig. 6 (upper panel). Alternatively, we calculate the electronic structure at the Γ point where the lowest unoccupied state has e' character to obtain Fig. 6 (lower panel). The ab-initio values of $\varepsilon_{\text{core}}(R)$ and $\ln[\varepsilon_{\text{core}}(R) - \varepsilon_{\text{core}}(\infty)]$ are fit quite well with (1b) with an effective Bohr radius of $a_0^* \sim 5.4 \text{ \AA}$ and $\epsilon_r = 20$ for the a'_1 hole and $a_0^* \sim 8.7 \text{ \AA}$ and $\epsilon_r = 13$ for the e' hole. The values of ϵ_r should be compared to recent calculations for the in-plane “macroscopic” dielectric constant where $\epsilon_r = 15$ was found for monolayers of MoS₂ as well as for bulk MoS₂ with negligible ionic contribution to the screening.⁷⁰ The deviation of $\epsilon_r = 20$ from the macroscopic value is not very surprising in view of the localization of the a'_1 hole that does not “see” many unit cells of MoS₂. The value for the e' hole is reasonable.

At large values of R in Fig. 6, the potential felt by the core states is seen not to decay but to oscillate. We attribute this to the accumulation of the residual hole charge at the supercell boundary that is a consequence of charge neutrality. The data points in Fig. 6 that deviate from the trend line are to be found outside the circle inscribed in the hexagonal WS cell.

In the effective mass approximation the effective Bohr radius $a_0^* = \epsilon_r/m_h \times 0.529 \text{ \AA}$ and the ground state binding energy with respect to the appropriate VBM is $\varepsilon_b = m_h/\epsilon_r^2 \times 13.606 \text{ eV}$. From the band structure in Fig. 1, the effective mass in units of the free electron mass m_0 is $m_h \sim 0.56$ at the K point VBM and 3.42 at the Γ point VBM, consistent with a previous calculation.⁷¹ Combining these masses with $\epsilon_r = 15$ ⁷⁰ leads to values of $a_0^* \sim 14 \text{ \AA}$ and $\varepsilon_b \sim 34 \text{ meV}$ for e' holes and $a_0^* \sim 2.3 \text{ \AA}$ and $\varepsilon_b \sim 207 \text{ meV}$ for a'_1 holes, respectively. At best the EMT is indicative but is clearly not quantitative for the most strongly bound acceptor states - a conclusion that is not especially surprising in view of the expected central cell correction for ground states⁶³ as well as the strong localization of both states.

The screening of the impurity potential by (i) the MoS₂ valence electrons and (ii) by the bound impurity hole means that the residual perturbation measured by the core states decreases rapidly with R allowing us to estimate the position of the reference core state far from the impurity and therefore of the VBM to an accuracy of a few meV for $N = 12$. This procedure was used to estimate the position of the VBM and of the impurity states with respect to it for each supercell size shown in Fig. 4 (dot-dashed line).

The same results can be obtained more simply by noting that the repulsive potential that binds a Rydberg series to the top of the valence band has little effect on the conduction band edge. Since we know the value of the band gap, the VBM can be determined from the conduction band minimum. We verified that this leads to the same results as the more elaborate procedure discussed in the foregoing.

2. Hydrogenic perturbation model

Now that we have established procedures for determining the position of the VBM, we see that the a'_1 and e' impurity bands in Fig. 4 not only narrow as the supercell size N is increased but rise with respect to the VBM. To make this clearer, we plot their centers of gravity

$$\bar{\varepsilon}_i = \frac{\sum_{n\mathbf{k}} f_{in}(\mathbf{k}) \varepsilon_n(\mathbf{k})}{\sum_{n\mathbf{k}} f_{in}(\mathbf{k})} \quad (2)$$

with respect to the VBM in Fig. 7; both levels are seen to rise as a function of N . The probability $f_{in}(\mathbf{k})$ is the i character of the wavefunction $\psi_{n\mathbf{k}}$ obtained by projecting $\psi_{n\mathbf{k}}$ onto site centered orbitals β_i and $i \equiv Rlm$ is a composite site, angular momentum index. Here we have chosen i to be the $d_{x^2-y^2}$ and d_{xy} Kubic harmonics on

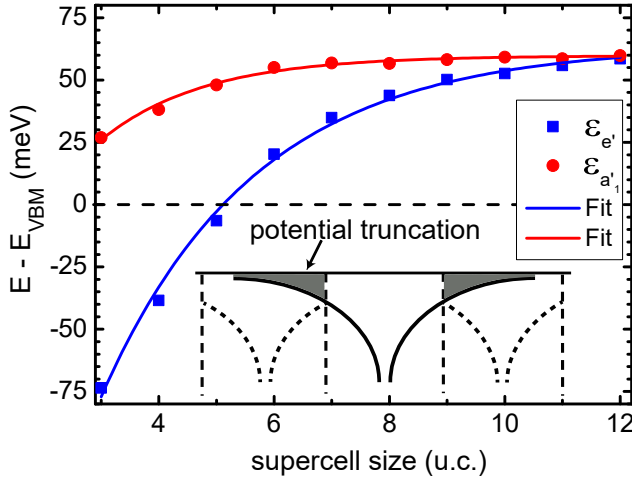


FIG. 7. Dependence on the supercell size N of the (spin-degenerate) a'_1 and e' impurity levels induced by a substitutional vanadium atom V_{Mo} with respect to the valence band maximum. The solid lines are fits to the data points using a model that includes the tail of the Coulomb potential in first order perturbation theory. (Inset) Truncation of the Coulomb potential in a supercell calculation.

the V_{Mo} atom for the e' state and $d_{3z^2-r^2}$ on V_{Mo} for the a'_1 state and the summation is carried out over the entire Brillouin zone and over the three split off impurity bands in Fig. 4. Since the position of the impurity levels introduced by V_{Mo} atoms will play an important role in determining the magnetic moment and exchange interaction between impurities, we wish to understand this increase.

A Coulomb potential in a semiconductor gives rise to a Rydberg series of bound states. A finite supercell cannot describe the asymptotic form of the potential correctly but will truncate it on the supercell boundary. In a self-consistent calculation, the requirement of charge neutrality will lead to the charge in the tail of the hydrogenic state accumulating on the supercell boundary. As the supercell size is increased, more of the “tail” of the (repulsive) Coulomb potential is described correctly, leading to the rise of the impurity levels seen in Figs. 4 and 7.

The effect of truncating the Coulomb potential can be estimated using a simple two dimensional (2D) hydrogenic⁶⁹ model and first order perturbation theory. For simplicity we assume a circular geometry and replace the 2D Wigner-Seitz cell with a circle of radius S with the same area $\pi S^2 = A_{WS}$. The correction to the ground state energy of a hydrogen atom in 2D is

$$\int_S^\infty R^2(r) \frac{e^2}{4\pi\epsilon_r r} 2\pi r dr = \frac{e^2}{2\pi\epsilon_r a_0^*} e^{-2S/a_0^*} \quad (3)$$

where a_0^* is the effective Bohr radius, ϵ_r is the relative dielectric constant and $R(r)$ is the radial part of the 2D hydrogenic wave function⁶⁹ for a screened Coulomb potential. Taking the top of the valence band ϵ_{VBM} of an

ideal MoS_2 monolayer, as estimated in the previous subsection, to be zero, we fit the ab-initio calculated data points with the solid curves shown in Fig. 7. The fit is very good and deviations can be attributed to local screening effects in the “real” inhomogeneous crystal as modelled in DFT.

The a'_1 and e' impurity levels increase in energy with increasing supercell size and converge to a (coincidentally) common value of ~ 62 meV in the single impurity limit ($N \rightarrow \infty$). From the fitting, we obtain another estimate of the effective Bohr radius of 8.3 \AA for the e' state, of 5.5 \AA for the a'_1 state and of $\epsilon_r \sim 10.0$ for the in-plane dielectric constant. These values should be compared to the EMT predictions of $a_0^* \sim 14 \text{ \AA}$ and $\epsilon_b \sim 34$ meV with respect to the K point VBM for the e' holes and $a_0^* \sim 2.3 \text{ \AA}$ and $\epsilon_b \sim 207$ meV with respect to the Γ point VBM for the a'_1 holes. Taking the LDA value of $\Delta_{K\Gamma} \sim 150$ meV from Table I into account, we would expect to find the a'_1 ground state at $207 - 150 = 57$ meV above the K point VBM.

According to Fig. 7, the highest e' impurity states emerge from the valence band when the supercell size is larger than 5×5 . This is consistent with the effective Bohr radius of the impurity levels deduced in Fig. 5. For impurity states with higher principal quantum numbers, the Bohr radii are at least twice as large. These states are not sufficiently localized in the Coulomb potential to appear above the valence band maximum for the largest supercells we have studied.

We can also determine effective Bohr radii from the dependence of the widths of the impurity bands, shown in Fig. 4, on the supercell size N because of the dependence of the bandwidth on the overlap of impurity wavefunctions in neighboring supercells. In Fig. 8 we plot the

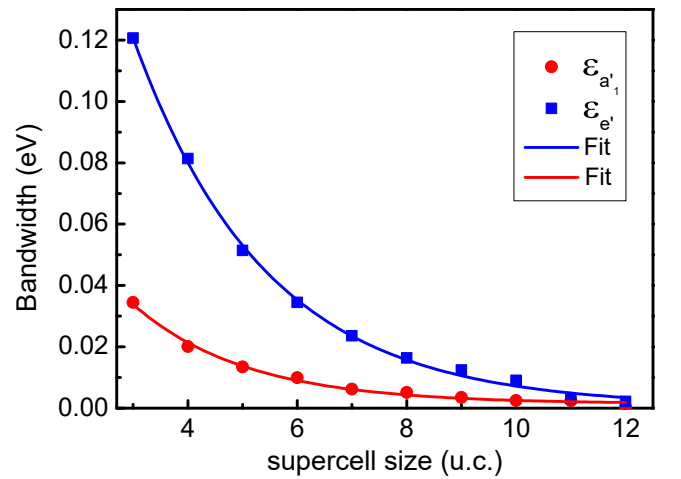


FIG. 8. Dependence of the band width of (spin-degenerate) impurity bands induced by substitutional V impurities on the supercell size N . The data points calculated using (4) are fit using the hydrogen model discussed in the text.

TABLE II. Summary of the a'_1 and e' bound state effective Bohr radii a_0^* (Å) derived in different ways without relaxation.

	V		Nb		Ta	
	$a'_1(\Gamma)$	$e'(\text{K})$	$a'_1(\Gamma)$	$e'(\text{K})$	$a'_1(\Gamma)$	$e'(\text{K})$
Fig. 5	4.2	8.0	5.3	10.0	5.2	10.3
Fig. 6, Eq. 1b Mo	5.4	8.7	6.2	9.6	5.8	9.7
Fig. 29, Eq. 1b S	6.5	8.8	6.8	10.0	6.5	10.0
Fig. 7, Eq. 3	5.5	8.3	5.9	10.0	6.2	10.4
Fig. 8, Eq. 4	5.2	7.8	5.2	9.8	5.4	10.1
EMT ($\epsilon_r = 15$)	2.3	14.0	2.3	14.0	2.3	14.0

second moment of the impurity bands

$$\sqrt{\frac{\sum_{n\mathbf{k}} f_{in}(\mathbf{k})(\varepsilon_n(\mathbf{k}) - \bar{\varepsilon}_i)^2}{\sum_{n\mathbf{k}} f_{in}(\mathbf{k})}} \propto e^{-R/a_0^*} \quad (4)$$

as a function of N where a_0^* is the effective Bohr radius and R is the distance between dopants in neighboring supercells. From the fitting, we get effective Bohr radii of 7.8 Å for the e' state and 5.2 Å for the a'_1 state which are consistent with our earlier results summarized in Table II.

3. Effect of relaxation

One of the most attractive and useful features of a plane wave basis is the ease with which Hellmann-Feynman forces can be calculated. This makes it simple to determine how the host MoS₂ crystal relaxes locally in response to substituting a Mo atom with V, Fig. 9. According to the electronic structure Fig. 4(d) for the unrelaxed geometry, shown enlarged in Fig. 10(b), the Fermi level is essentially pinned in the orbitally nondegenerate a'_1 state and the system does not undergo a Jahn-Teller (JT) distortion; if we begin geometry optimisation from a JT distorted configuration, the system relaxes back to a symmetric one. Consistent with this,

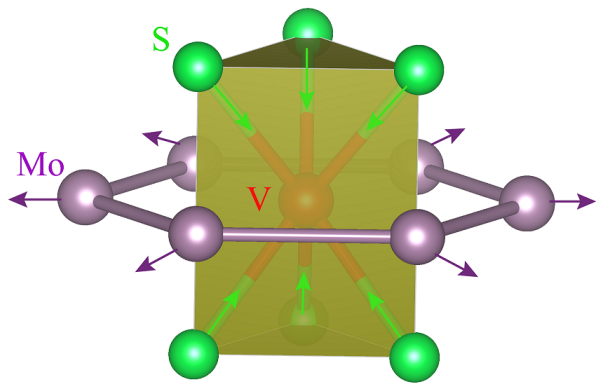


FIG. 9. (color online). Schematic of the relaxation about a vanadium atom on a substitutional Mo site, V_{Mo} , in MoS₂.

TABLE III. Relaxation of nearest neighbour S and Mo shells about a substitutional vanadium atom as a function of the $N \times N$ supercell size N . Atomic displacements in Å.

N	3	6	9	12	15
Δd_{V-S}	-0.060	-0.060	-0.060	-0.060	-0.060
Δd_{V-Mo}	0.003	0.005	0.008	0.008	0.008

we find only symmetry-conserving (“breathing mode”) relaxation about the vanadium ion with the six nearest neighbour sulphur atoms relaxing towards the V atom and the six in-plane neighbouring Mo atoms relaxing radially away, shown in Fig. 9. The displacements converge rapidly with supercell size to $\Delta d_{V-S} = 0.060$ Å and $\Delta d_{V-Mo} = 0.008$ Å as seen in Table III. The total energy gain from relaxation is 150 meV.

The band structures of the unrelaxed and relaxed 12×12 impurity supercells are compared in panels (b) and (d) of Fig. 10. The band structures are aligned on the VBM, located at the Γ point as seen in Fig. 10(a) for an undoped monolayer, using the $4s$ semicore level shift of the “B4” Mo atom on the boundary of the Wigner-Seitz cell furthest from the dopant V atom, see Fig. 3. The main effect of relaxation is to lift the quasidegeneracy of the a'_1 and e' impurity states, Fig. 10(d). The increased V-Mo bond length leads to a lowering of the center of gravity of the e' state with respect to the a'_1 state that is antibonding with respect to the neighbouring S p states. As a consequence, the hole state acquires essentially pure a'_1 character.

4. Spin polarization

The electronic structure of an unpaired spin in an orbitally nondegenerate a'_1 impurity state resembles that of a free hydrogen-like atom and, like a free atom, its total energy can be lowered by allowing the electron to polarize in the local spin density approximation.^{67,72} The result of doing so in the dilute limit is shown in Figs. 10(c) and (e). Without relaxation, the localized and dispersionless a'_1 state splits by 91 meV leaving the hole with mixed a'_1 - e' character and a magnetic moment of $m = 1\mu_B$. Expressing the exchange splitting in terms of an effective Stoner parameter I_{xc} as $\Delta\varepsilon = mI_{xc}$ results in a value of I_{xc} of 91 meV that is substantially less than the free atom value of $I_{xc} \sim 0.7$ eV.⁷³ In the local density approximation, it is the local electron density that drives the exchange splitting and the small exchange splitting can be understood in terms of the much lower spin density of the impurity state compared to that of a free atom. Consistent with this picture is the even smaller exchange splitting of the more delocalized e' state that is only ~ 25 meV. Before relaxation, the partial occupation of a'_1 and e' states allows the e' state to “freeload” on the much more localized a'_1 electron density enhancing its spin polarization and exchange splitting (24.7 meV) which decreases to 15.2 meV

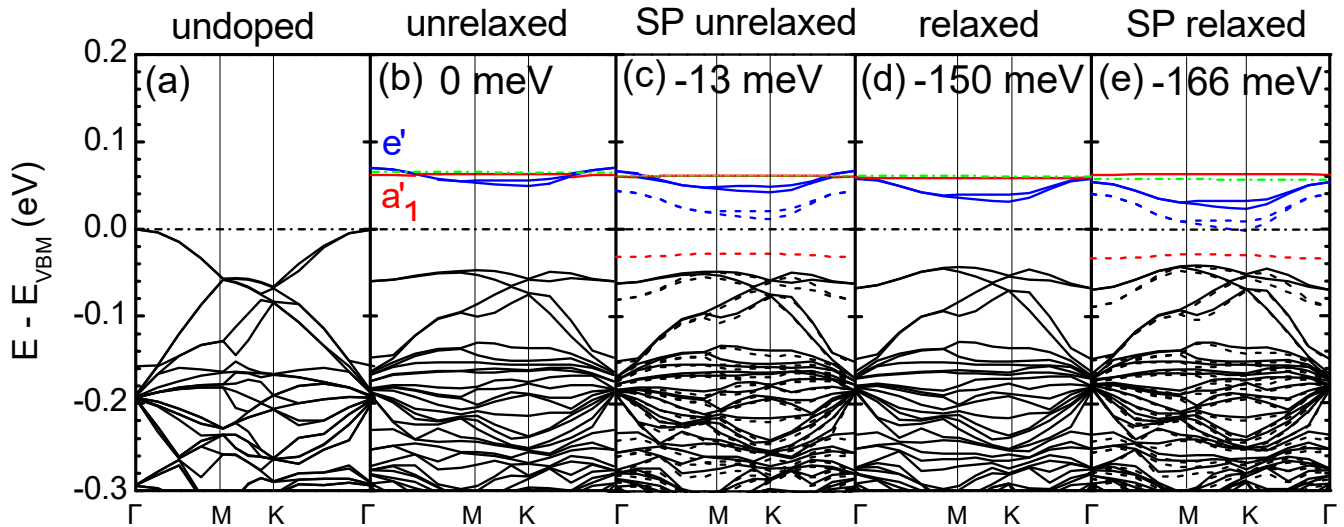


FIG. 10. Effect of relaxation and spin-polarization on the electronic structure of a 12×12 supercell for an MoS₂ monolayer with a single Mo atom replaced by V. (a) Reference bands for an undoped MoS₂ monolayer, energy bands for a single substitutional V impurity (b) without relaxation, (c) with spin polarization (SP) and without relaxation, (d) with relaxation, without spin polarization, (e) spin polarized and relaxed. The a'_1 level is red, the e' states are blue. In (c) and (e), the solid (dashed) lines indicate minority (majority) spin states. The energy gain with respect to the unrelaxed case is given in each panel in meV. The zero of energy is the VBM and the Fermi level is indicated by a green dot-dashed line.

after relaxation, Table VI. The mixing of the e' impurity state with what will eventually become the top of the valence band is clearly seen in the 12×12 supercell in terms of the large exchange splitting of the uppermost host valence band state (black solid and dashed bands) at the Γ point. The total energy gain from spin polarization of 13 meV without relaxation or 16 meV with relaxation is dwarfed by the 150 meV energy gain from relaxation.

For smaller supercell sizes, the dispersion of the e' state increases until it overlaps the unoccupied a'_1 level and begins to quench the spin polarization for $N < 8$, Table IV. Reducing the supercell size further increases the quenching and when, in addition, the impurity potential fails to pull the impurity levels above the VBM for supercell sizes

TABLE IV. Calculated magnetic moment (in μ_B) for an MoS₂ monolayer supercell doped with V, Nb and Ta as a function of the $N \times N$ supercell size without (Un) and with (Re) relaxation. For V the effect of an onsite Coulomb repulsion parameter $U = 1$ eV was examined for the relaxed case. The reciprocal space sampling density is constant.

N		3	4	5	6	7	8	9	10	11	12
V	Un	0.00	0.00	0.61	0.82	0.97	1.00	1.00	1.00	1.00	1.00
	Re	0.00	0.00	0.81	1.00	1.00	1.00	1.00	1.00	1.00	1.00
	U	0.54	0.68	1.00	1.00	1.00	1.00	1.00	1.00	1.00	1.00
Nb	Un	0.00	0.00	0.00	0.34	0.54	0.68	0.87	0.93	1.00	1.00
	Re	0.00	0.00	0.00	0.66	0.75	0.89	1.00	1.00	1.00	1.00
Ta	Un	0.00	0.00	0.00	0.32	0.42	0.57	0.86	0.95	1.00	1.00
	Re	0.00	0.00	0.00	0.68	0.83	0.92	1.00	1.00	1.00	1.00

smaller than 5×5 , the magnetic moment disappears. Relaxation enhances the magnetic moment by reducing the overlap of the a'_1 and e' states in spite of the unfavourable increase of the e' state dispersion. Even a very small value of the Coulomb repulsion parameter $U = 1$ eV⁷⁴ can lead to a 3×3 supercell becoming polarized. Most of the discrepancies in the literature can be explained in terms of the supercell size, k-point sampling, exchange-correlation potential, U etc.^{28,33,36,39,42,44,49,50,75}

5. Formation energies

The formation energy of a substitutional dopant X_{Mo} is defined as

$$E_{\text{form}}[X_{\text{Mo}}] = E_{\text{tot}}[\text{MoS}_2:X] - E_{\text{tot}}[\text{MoS}_2] + \mu_{\text{Mo}} - \mu_X \quad (5)$$

where $E_{\text{tot}}[\text{MoS}_2:X]$ is the total energy of an MoS₂ monolayer with one Mo atom replaced by one X atom, $E_{\text{tot}}[\text{MoS}_2]$ is the total energy of a pristine MoS₂ monolayer and μ_{Mo} and μ_X are the total energies per atom

TABLE V. Formation energies in eV of substitutional V, Nb and Ta impurities in an MoS₂ monolayer for a 12×12 supercell.

	V	Nb	Ta
Unrelaxed	0.40	0.01	-0.12
Relaxed	0.25	-0.15	-0.23

of Mo and X in their bulk metallic bcc phases, respectively. Taking the (spin-polarized) S_2 molecule as the reference chemical potential for S, the heat of formation of a MoS_2 monolayer, $E_{\text{form}}[\text{MoS}_2]$, was calculated to be -5.31 eV/formula unit. The formation energy of V_{Mo} is small and those of Nb_{Mo} and Ta_{Mo} actually become negative when relaxed indicating that doping MoS_2 with these group V elements should be experimentally feasible, Table V.

B. Binding of V impurity pairs

Two substitutional dopant V atoms will have a negligible interaction energy when sufficiently far apart. This energy can be calculated as follows. First define a reference energy E_V^N for a single V dopant atom substituting a Mo atom in MoS_2 as

$$E_V^N = E_{\text{tot}}^N[V_{\text{Mo}}] - E_{\text{tot}}^N[\text{MoS}_2] \quad (6)$$

where $E_{\text{tot}}^N[\text{MoS}_2]$ is the total energy of an $N \times N$ supercell of MoS_2 in equilibrium and $E_{\text{tot}}^N[V_{\text{Mo}}]$ is the total energy of the same supercell with one Mo atom replaced with a V atom. To calculate absolute formation energies, suitable chemical potentials would need to be included to take account of where the V atom came from and where the Mo atom went to; we will not be concerned with those here. The binding energy E_b is then

$$E_b^N(R) = E_{\text{tot}}^N[V_2(R)] - E_{\text{tot}}^N[\text{MoS}_2] - 2E_V^N \quad (7)$$

where $E_{\text{tot}}^N[V_2(R)]$ is the total energy of a supercell with two Mo atoms a distance R apart substituted with V atoms and the last two terms on the right do not depend on R . We consider the two cases where relaxation is (Re) and is not (Un) included.

For supercells containing two substitutional V atoms as far apart as possible (R_{max}), with one V atom at the origin and the second at the corner site in Fig. 3, the binding energy $E_b^N(R_{\text{max}})$ is shown as a function of the supercell size N in Fig. 11 with spin polarization included. Although $E_b^N(R_{\text{max}})$ does not change much for $N \geq 12$, there is still a surprisingly large binding energy of ~ 8 meV for $N = 15$ in the unrelaxed case. We can trace this to the near degeneracy of the minority-spin e' and a'_1 related bands shown in Fig. 10(c) for the unrelaxed V_{Mo} as well as the relatively long range of the e' holes. When relaxation is included, the hole becomes localized in the dispersionless minority-spin a'_1 band, Fig. 10(e), it becomes much easier to converge the total energy (with respect to BZ sampling and self-consistency) and $E_b^{12}(R_{\text{max}})$ decreases fast to ~ 2 meV for $N = 12$. In general, when there is a gap between occupied and unoccupied states, total energies can be converged better. Since the problem has to do with the (separation independent) reference energy E_V^N , it turns out to be better to consider

$$E_b^N(R) = E_{\text{tot}}^N[V_2(R)] - E_{\text{tot}}^N[V_2(R = \infty)] \quad (8)$$

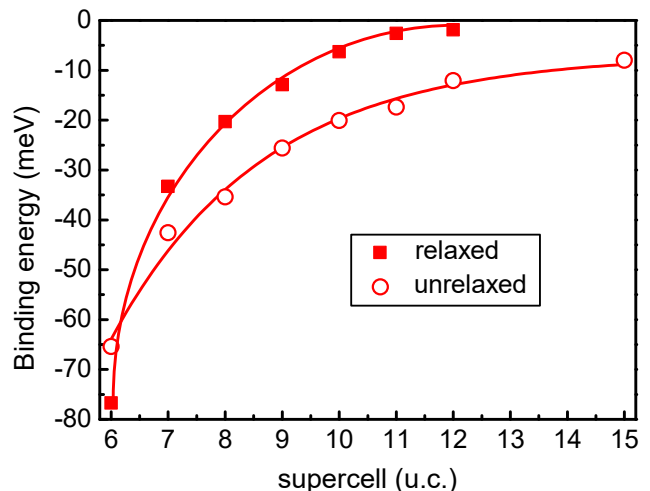


FIG. 11. $E_b^N(R_{\text{max}})$ as a function of the supercell size N for spin-polarized unrelaxed (open red circles) and relaxed (filled red squares) geometries. The red lines are a guide for the eye.

and approximate $E_{\text{tot}}^N[V_2(R = \infty)] \sim E_{\text{tot}}^N[V_2(R_{\text{max}})]$

Using a 12×12 supercell and (8) we explore the pair binding energy $E_b^{12}(R)$ for V_{Mo} dopants as a function of their separation R in Fig. 12 where one dopant atom is assumed at the site marked 0 in Fig. 3. Without relaxation, the (absolute value of the) binding energy de-

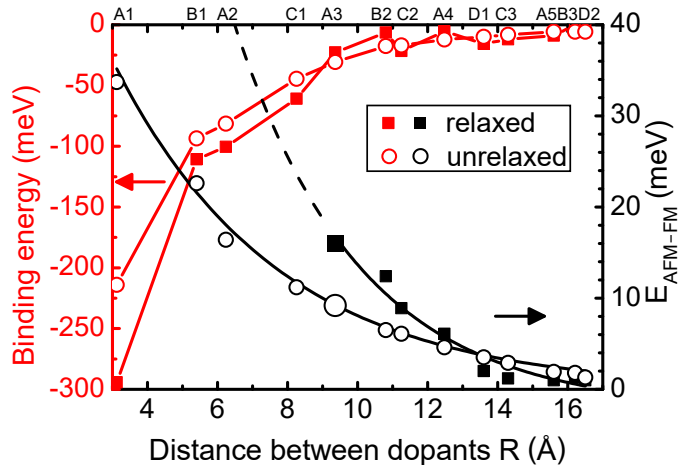


FIG. 12. Red symbols: interaction energies of dopant V_{Mo} atoms in a 12×12 MoS_2 supercell as a function of their separation. The binding energy was calculated using (8) for unrelaxed (open red circles) and relaxed (filled red squares) geometries. The lines are a guide to the eye. Black symbols: total energy differences between parallel and antiparallel aligned spins on the V dopant atoms without (open black circles) and with (filled black squares) relaxation. The lines are fits to an exponentially decaying function. The dashed black line extrapolates the relaxed exchange interaction to separations where it is found to be quenched. The labels along the top of the figure indicate the sites in Fig. 3 and the large symbols refer to the A3 configuration discussed in the text and Fig. 16.

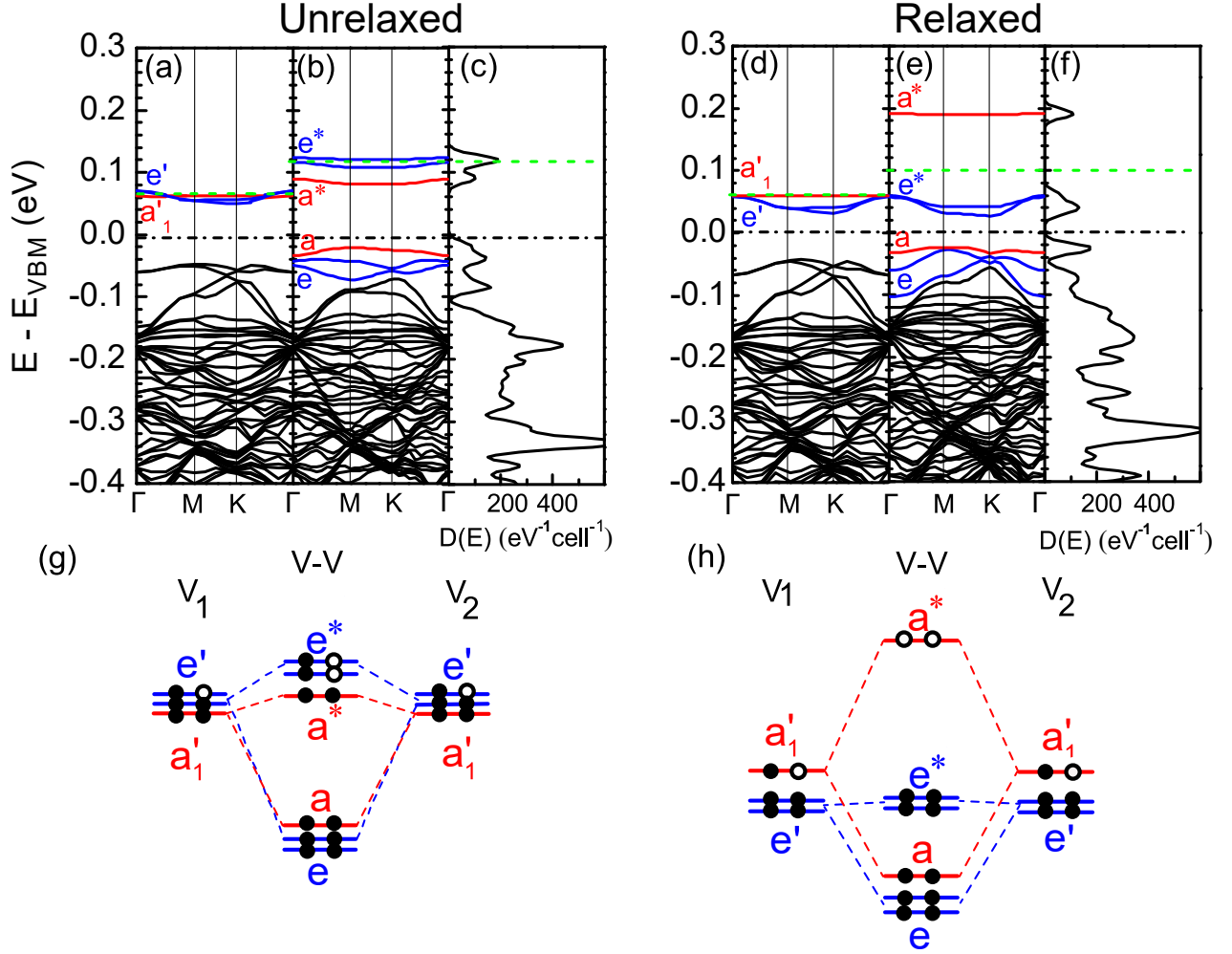


FIG. 13. Spin unpolarized electronic structure (bands and DoS) for a 12×12 MoS₂ supercell with two V atoms in an A1 configuration on nearest neighbour Mo sites (b,c,e,f) and, for comparison, for a single V_{Mo} atom (a,d) corresponding to Fig. 10(b,d). Without (a,b,c,g) and with (d,e,f,h) atomic relaxation. Schematic of the coupling mechanism between two V dopants with two holes without (g) and with (h) atomic relaxation. Impurity bands are highlighted in red and blue. The K point VBM is set to be zero (dot-dashed black line) and the Fermi level is shown as a dashed green line.

creases monotonically from a value of ~ 220 meV for V atoms on neighbouring Mo sites to a value of ~ 0 meV at the maximum separation in a 12×12 supercell (open red circles, left axis). Because these energies are so small, we will later assume that dopant atoms are randomly distributed in real materials that are not in full thermodynamic equilibrium.

With relaxation (filled symbols), the magnitude of the binding energy increases for separations R smaller than a critical separation, $R_c \sim 8.5 \text{ \AA}$, and does not change for separations larger than this. This behaviour is intimately related to quenching of the magnetic moments for V dopant atoms closer than R_c and for these separations, $R < R_c$, an exchange interaction cannot be determined. We proceed to consider the magnetic interactions.

C. Magnetic Interaction of impurity pairs

We estimate the exchange interaction $\Delta E(R)$ between pairs of dopant atoms as the energy difference between configurations with the V magnetic moments aligned parallel (“ferromagnetically”, FM) and antiparallel (“antiferromagnetically”, AFM)

$$\Delta E(R) = E_{\text{tot}} [V_2^{\text{AFM}}(R)] - E_{\text{tot}} [V_2^{\text{FM}}(R)] \quad (9)$$

in 12×12 supercells so that the interaction between periodic images is acceptably small. Because the spin-polarized calculations are computationally expensive, care is taken to construct suitable starting V_2^{FM} configurations using “superpositions” of relaxed, spin-polarized local atomic configurations for single V_{Mo} . Starting V_2^{AFM} configurations are constructed from relaxed V_2^{FM} configurations so only the much smaller differential re-

laxation needs to be calculated.

The energy difference between antiferromagnetic and ferromagnetic ordering without (open black circles) and with (filled black squares) relaxation is shown on the right axis of Fig. 12. Before relaxation, neighbouring V dopant atoms show FM coupling with a total moment of $2\mu_B$ or $1\mu_B$ per V for all separations. The interaction decreases monotonically and exponentially from a maximum of ~ 33 meV for nearest neighbours with a decay length of ~ 5.3 Å. With relaxation included the magnetic moments are quenched for separations R smaller than a critical separation, $R_c \sim 8.5$ Å, and for these separations an exchange interaction cannot be determined. For separations $R > R_c$, the coupling remains ferromagnetic and is enhanced. Because the maximum value of the magnetic ordering temperature will depend strongly on this relaxation-induced behaviour, we need to understand its origin.

1. Quenching of moments for $R < R_c$

To do so, we consider a 12×12 supercell for an MoS₂ monolayer with a pair of Mo atoms on neighbouring sites substituted with V. The unpolarized supercell electronic structures and DoS are shown in Fig. 13 without (left) and with relaxation (right). The correspond-

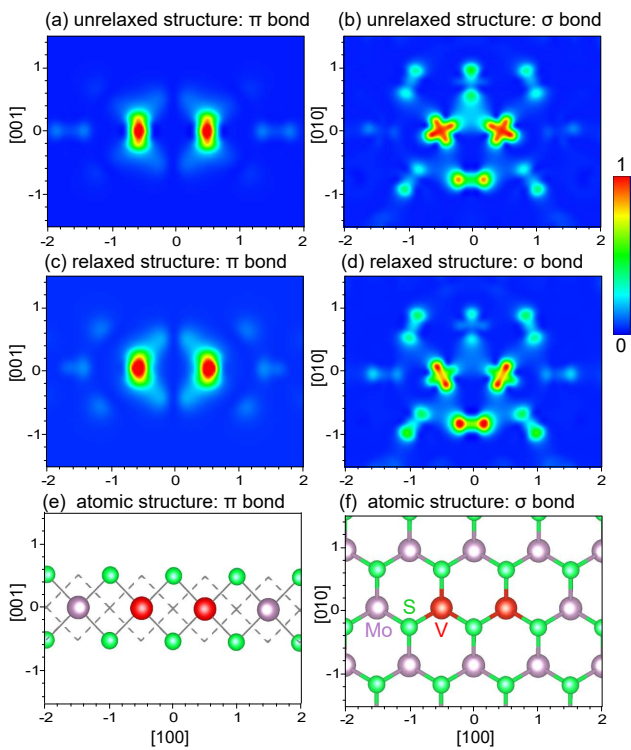


FIG. 14. Side view of the partial charge distributions of the π bond (left panels) and top view of the σ bond (right panels) without (a, b) and with (c, d) atomic relaxation. The corresponding atomic structures are shown in (e, f).

ing band structures for a single V impurity are included in the left panels for reference. In the spirit of a defect molecule model, Fig. 13(a-c) suggests that the e' orbitals form σ bonding-antibonding $e-e^*$ pairs scarcely lifting the degeneracy of the e states while the a'_1 states interact less strongly to form a π bonding-antibonding $a-a^*$ pair. Without relaxation, the strength of the π bond between the a'_1 orbitals is not strong enough to raise the a^* level above the e^* level and the two holes reside on the four-fold orbitally and spin degenerate e^* states as sketched in Fig. 13(g). This leads to a DoS peak at the Fermi level that is unstable with respect to exchange splitting.

Relaxation results in a structure where the neighbouring S atoms move closer to the V atoms, the two V atoms move apart and the a'_1 levels on individual V_{Mo} atoms are lifted clear of the e' levels. The reduced V-S separation strengthens the π bond [Fig. 14(a) versus Fig. 14(c)] through hybridization between vanadium $d_{3z^2-r^2}$ and sulphur p_x and p_y orbitals, while the σ bonds formed by vanadium $\{d_{xy}, d_{x^2-y^2}\}$ orbitals are weakened by the increased V-V separation [Fig. 14(b) versus Fig. 14(d)]. This makes the π bond the dominant bonding interaction between dopants. The $a-a^*$ splitting is increased so much by relaxation that the a^* level is lifted well above the e^* level and the two holes are accommodated in an orbitally nondegenerate state (rhs of Fig. 13).

To demonstrate how competition between bonding and exchange interactions of the V $d_{3z^2-r^2}$ orbitals leads to the quenching of the magnetic moments, we examine how these interactions depend on the separation between the dopant atoms. We define the bond strength Δ_π of the π bond to be the a^*-a bonding-antibonding splitting. Fig. 15 shows how Δ_π depends on the impurity separation R with (filled black squares) and without (open black circles) structural relaxation. As R increases, Δ_π decreases because of the decreasing wavefunction overlap. Without relaxation (open circles), Δ_π is smaller than the exchange splitting (red triangles, dashed red line) for all separations and a triplet state would form as indicated in the rhs inset of Fig. 15. With relaxation (filled squares), Δ_π is larger and exceeds the exchange splitting at distances smaller than ~ 7 Å. A singlet state is formed to gain bonding energy, as sketched in the lhs inset of Fig. 15, and this leads to the quenching of the magnetic moment. The critical quenching separation is twice the effective Bohr radius $a_0^* = 4.2$ Å for the a'_1 state, implying the formation of a π bond. In general, to quench the magnetic moment, the π bonding interaction should be strong enough to make the a^* state the highest lying state.

Lastly, we note a significant enhancement of the exchange splitting when two vanadium atoms are close, Fig. 15. From a value of 92 meV for single V dopants, the increase in hole density at short separations doubles the exchange splitting to ~ 180 meV for (unrelaxed) V dopants on neighbouring Mo sites.

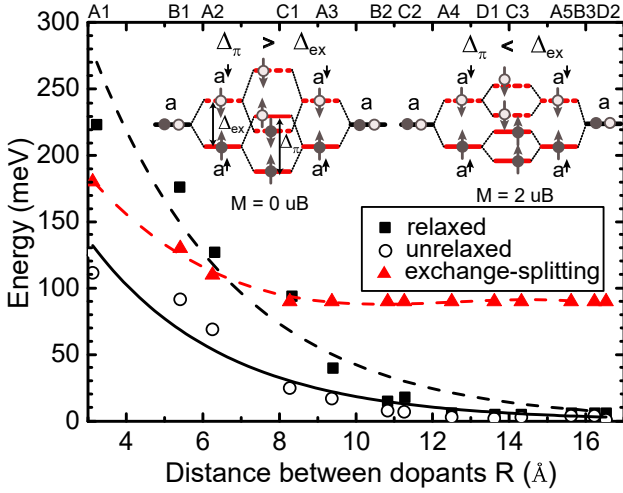


FIG. 15. Unpolarized $a - a^*$ level separation with (filled black squares) and without (open black circles) atomic relaxation plotted as a function of the separation between the substitutional dopant atoms in a 12×12 MoS₂ supercell. The a^* exchange splitting for different (unrelaxed) configurations is indicated by red triangles. The insets show the energy level schemes with spin polarization included for relaxed configurations with impurity separations below (lhs) and above (rhs) the critical separation of 8.5 Å, respectively.

2. Enhancement of Exchange Interaction for $R > R_c$

For separations greater than R_c , the exchange interaction is strongly enhanced by relaxation before decaying more strongly than the unrelaxed case till it eventually becomes smaller when $R \sim 13 \text{Å}$, Fig. 12. We can understand the enhancement by considering in Fig. 16 the defect levels associated with the A3 configuration, Fig. 3. For the unrelaxed structure (lhs), the breaking of the local D_{3h} symmetry is negligible and the bonding e and antibonding e^* states remain doubly degenerate. At this separation of 9.55 Å, the bonding interaction of the a'_1 states is much less that of the e' states so that the e^* level is the lowest unoccupied level to which both holes gravitate. Because it is degenerate, the e^* level can exchange split with both holes aligned to form a triplet spin state. The exchange splitting is weak because of the delocalisation of the e levels.

Relaxation reduces the V-S bond length while increasing the V-V bond length and breaks the local D_{3h} symmetry leading to a significant splitting of the degenerate e and e^* levels as well as a small increase in the bonding interaction between the a'_1 levels (Fig. 16, rhs). The net result is that the a^* level and highest e^* level become degenerate and accommodate the two holes. Because of the greater localization of the a levels, this leads to an enhancement of the exchange splitting for the parallel (FM) configuration of the two V_{Mo} dopants (compared to the unrelaxed case) and a reduction for the antiparallel (AFM) configuration with a corresponding increase of the $E_{\text{AFM}} - E_{\text{FM}}$ energy difference (large symbols in Fig. 12).

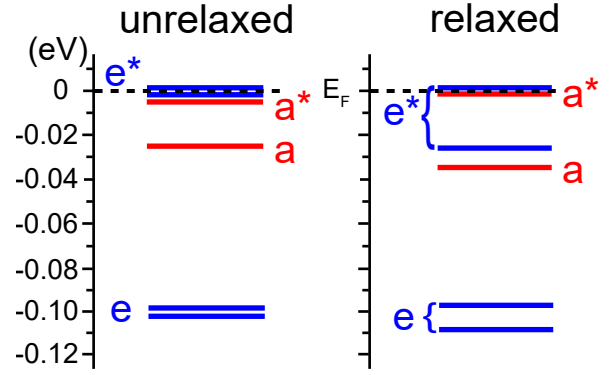


FIG. 16. Defect level structure calculated without spin polarisation for an A3 configuration of two V_{Mo} atoms. (lhs) unrelaxed and (rhs) relaxed. The levels are calculated from the appropriate weighted average of the Γ , K/K' and M eigenvalues of the corresponding bands. a and a^* (red), e and e^* (blue) levels originate in the a'_1 and e' levels for single V_{Mo} dopants. The zero of energy is the Fermi level indicated by a black dashed horizontal line.

To a good approximation the interaction strength only depends on the separation and decays exponentially more rapidly than the unrelaxed case with a much reduced decay length of 3.6 Å reflecting the greater localization of the a'_1 holes.

D. Nb and Ta in MoS₂

We expect Nb and Ta to more closely resemble Mo than V with a weaker central cell potential leading to less localized impurity states than in the case of V. Nb and Ta will turn out to have very similar effective Bohr radii and binding energies that lead to virtually indistinguishable magnetic properties.

1. Single impurity limit: Nb and Ta in MoS₂

For an unrelaxed Nb (Ta) substitutional impurity, we find an effective Bohr radius of 10.0 (10.3) Å for the e' state and 5.3 (5.2) Å for the a'_1 state by fitting the circularly averaged wave function in a 12×12 supercell to be compared to values of 8 Å and 4.2 Å, respectively, for V found in Sec. III A, Table II. The binding energies of these e' and a'_1 states converge to a common value of ~ 45 meV in the large supercell, single impurity limit Fig. 17; the results for Nb and Ta are virtually indistinguishable and only those for Nb are shown. The smaller binding energies and larger effective Bohr radii make the Nb (Ta) impurity states more sensitive to the supercell truncation of the impurity potential compared to V. Increasing delocalization of the holes from $V \rightarrow \text{Ta}$ leads to a reduction of the exchange splittings, Table VI, and a magnetic moment is found to develop only when $N > 5$.

TABLE VI. Summary of the exchange splitting Δ_{ex} in meV of a'_1 and e' bound states in unrelaxed (Un) and relaxed (Re) structures in 12×12 supercells.

Δ_{ex}	V		Nb		Ta	
	$a'_1(\Gamma)$	$e'(\text{K})$	$a'_1(\Gamma)$	$e'(\text{K})$	$a'_1(\Gamma)$	$e'(\text{K})$
Un	91.3	24.7	32.4	10.9	35.6	10.8
Re	96.1	15.2	53.2	9.8	52.0	9.7

Total polarization only occurs for $N > 10$, see Table IV.

After relaxation, the Nb-Mo (Ta-Mo) bond length increases by 0.040 (0.036) Å, leading to a lowering of the e' state. The hole then goes into the a'_1 state whose exchange splitting increases while that of the e' state decreases because of the reduced overlap in space of the e' and a'_1 partial electron densities. As we already saw for V in Table IV, relaxation enhances the magnetic moments.

2. Interaction of Nb (Ta) impurity pairs

Because of the smaller bound state energies and weaker spin polarization, the exchange interaction between pairs of Nb (Ta) dopant atoms is weaker than that between pairs of V atoms, Fig. 12, and decays more slowly with increasing separation, Fig. 18. To a good approximation the interaction strength only depends on the separation R and decays exponentially with R with a decay length of 5.2 (5.8) Å versus 3.6 for V when relaxation is included.

The exchange splitting of the a'_1 and e' levels and their relative hole occupations determine the strength of their different exchange interactions. Relaxation raises the a^* level to become degenerate with the upper e^* level, enhancing the exchange splitting of the a level while reducing that of the e level (see Table VI) and changes the character of the holes from e -like to $a+e$ -like. This increases the strength of the exchange interaction but leads

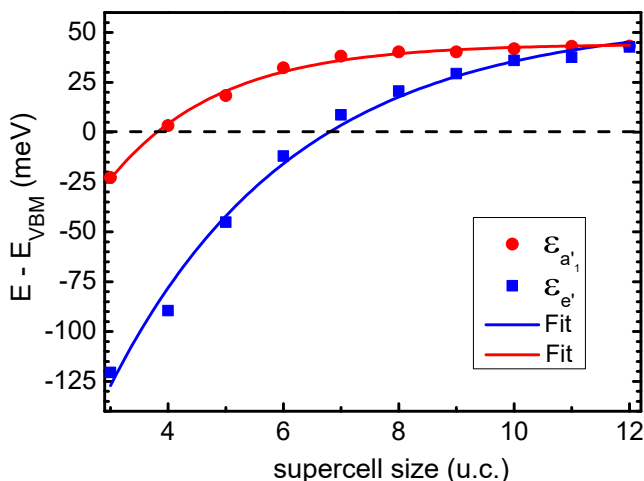


FIG. 17. Same as Fig. 7 but for Nb instead of V. The corresponding results for Ta are virtually indistinguishable.

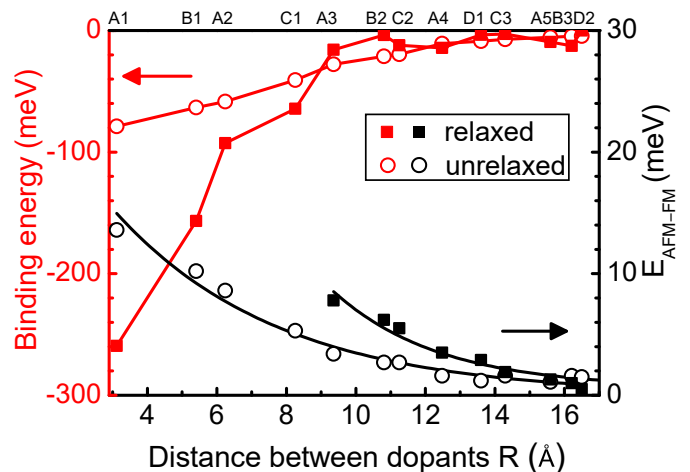


FIG. 18. Same as Fig. 12 but for Nb instead of V. The corresponding results for Ta are virtually indistinguishable.

to a faster decay as we saw in Figs 12 and 18 for vanadium.

In summary, before relaxation, the long-range weak e' ferromagnetic interaction dominates while the strong short-range a'_1 interaction dominates after relaxation, the near-degeneracy of the upper e^* and a^* levels making it possible to form a triplet without violating the Pauli exclusion principle.

IV. MAGNETIC ORDERING

The Ising spin model in two dimensions undergoes a phase transition to long-range magnetic order at a finite temperature.^{76,77} For a Heisenberg model with isotropic exchange interactions, thermal fluctuations destroy long-range magnetic ordering in two dimensions at any finite temperature.^{7,8} The Ising spin model, with spin dimensionality $n = 1$, is recovered by assuming a generalized Heisenberg spin Hamiltonian with isotropic exchange and strong perpendicular anisotropy. Though the predictions of such generalized Heisenberg models are not identical to those of the Ising spin model, the consensus is that for ferromagnetism to exist in two-dimensional systems, magnetic anisotropy is essential. We therefore begin this section on magnetic ordering by studying the magnetic anisotropy of a single substitutional dopant, the so-called single ion anisotropy (SIA).

A. Single ion anisotropy

Microscopically, magnetic anisotropy arises when spin and orbital degrees of freedom are coupled by the spin-orbit interaction so that the total energy depends on the spatial orientation of the magnetic moment. According to the “force theorem”,^{78,79} changes to the total energy, δE , that result from a small perturbation can be related

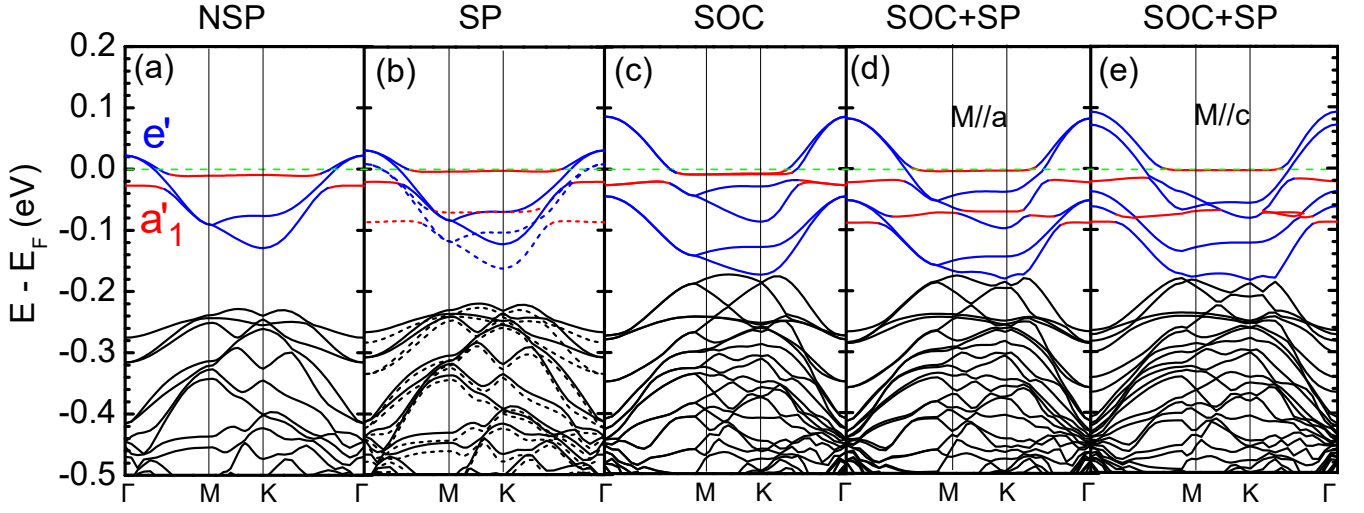


FIG. 19. The band structure of a single V dopant in a 6×6 supercell including relaxation. (a) non-spin polarized (NSP), (b) spin polarized (SP), (c) only spin orbit coupling (SOC). Including SOC and SP with the magnetization in-plane ($\mathbf{M} \parallel a$) (d) and perpendicular to the monolayer plane ($\mathbf{M} \parallel c$) (e). Because SOC does not mix the e' ($m_l = \pm 2$) and a'_1 ($m_l = 0$) states strongly, we can continue to label these blue and red. In (b), the solid and dashed lines represent spin-up and spin-down states, respectively. The Fermi level shown as a horizontal green dashed line is chosen to be zero.

to changes in the sum of the single-particle eigenstates of the Kohn-Sham equations⁸⁰ of DFT, $\delta E \sim \delta \sum_i^{\text{occ}} \varepsilon_i$, which should not be iterated to self consistency. The force theorem has been applied to the calculation of the magnetic anisotropy energy (MAE) where the perturbation is the spin-orbit coupling (SOC)⁸¹ and comparison with explicit total energy calculations yields essentially perfect agreement for Fe, Co and Ni.⁸² The advantage of the force-theorem approach is that it allows the MAE to be directly related to (changes to) the electronic structure^{83,84} which are shown for the relaxed configuration of a single V atom in a 6×6 supercell of MoS₂ in Fig. 19.

In the context of Fig. 10(e), we already discussed the exchange splitting of the a'_1 and e' levels. In a 6×6 supercell, the increased band dispersion leads to a smaller exchange splitting. With (without) relaxation, these splittings averaged over the Brillouin zone are, respectively, 66 (64) meV and 20 (22) meV (Fig. 19b). Because MX₂ monolayers do not have inversion symmetry, SOC leads to a substantial splitting of the spin degenerate states at K and K' with $\{d_{xy}, d_{x^2-y^2}\}$ character ($l = 2, m = \pm 2$).⁸⁵ In Fig. 19(c), we see that SOC splits the e' level at Γ by 130 meV while the a'_1 level with $d_{3z^2-r^2}$ character ($l = 2, m = 0$) is not affected. For a larger (12×12) supercell, the effect of SOC on the bands shown in Fig. 10(d) is to split the upper e' level so that it lies above the unaffected a'_1 level and accommodates the hole.

To understand the energy levels obtained with SOC and spin polarization (exchange splitting) in the single impurity limit, it is instructive to consider the model Hamiltonian

$$H = H_0 + \Delta \mathbf{m} \cdot \mathbf{s} + \xi \mathbf{l} \cdot \mathbf{s} \quad (10)$$

where H_0 is the spin-independent part of the Hamiltonian, $\Delta \mathbf{m}$ is the exchange field that leads to an exchange splitting Δ , and \mathbf{m} is a unit vector in the direction of the magnetization, $\mathbf{m} \equiv \mathbf{M}/|\mathbf{M}|$. In the subspace of the $l = 2, m_l = \pm 2$ orbitals

$$\xi \mathbf{l} \cdot \mathbf{s} = \frac{\xi}{2} \begin{pmatrix} l_z & l_- \\ l_+ & -l_z \end{pmatrix} = \begin{pmatrix} \xi & 0 \\ 0 & -\xi \end{pmatrix} \quad (11)$$

where we use Hartree atomic units with $\hbar = 1$. For $\mathbf{M} \parallel c$,

$$\Delta \mathbf{m} \cdot \mathbf{s} = \begin{pmatrix} \frac{\Delta}{2} & 0 \\ 0 & -\frac{\Delta}{2} \end{pmatrix}. \quad (12)$$

and the SOC Hamiltonian can be written as

$$H = H_0 + \begin{pmatrix} \xi + \frac{\Delta}{2} & 0 & 0 & 0 \\ 0 & -\xi - \frac{\Delta}{2} & 0 & 0 \\ 0 & 0 & -\xi + \frac{\Delta}{2} & 0 \\ 0 & 0 & 0 & \xi - \frac{\Delta}{2} \end{pmatrix} \quad (13)$$

For $\mathbf{M} \parallel a$ we have

$$H = H_0 + \begin{pmatrix} \xi & \frac{\Delta}{2} & 0 & 0 \\ \frac{\Delta}{2} & -\xi & 0 & 0 \\ 0 & 0 & -\xi & \frac{\Delta}{2} \\ 0 & 0 & \frac{\Delta}{2} & \xi \end{pmatrix}. \quad (14)$$

Diagonalizing H results in the energy level scheme sketched in Fig. 20. The magnetic anisotropy energy is $E_{\text{MAE}} = E_a - E_c$, where E_a and E_c are the total energies when $\mathbf{M} \parallel a$ and $\mathbf{M} \parallel c$, respectively. Using the force theorem, the energy change on including SOC is given by the change in the sum of single-particle eigenvalues. The reference energy (without SOC) cancels when the difference is taken for the two magnetization directions and,

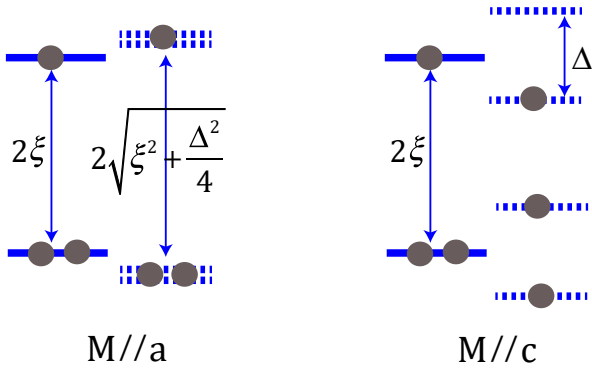


FIG. 20. Schematic of the e' energy levels with spin orientation in-plane ($\mathbf{M}\parallel a$) and out of plane ($\mathbf{M}\parallel c$). The solid blue lines are spin degenerate.

for occupancy with a single hole, E_{MAE} can be estimated to be

$$E_{\text{MAE}} = E_a - E_c = \xi + \frac{\Delta}{2} - \sqrt{\xi^2 + \frac{\Delta^2}{4}} \quad (15)$$

where we make use of the fact that the sum over all single particle eigenvalues is zero to express the sum over occupied states in terms of the sum over unoccupied states that is simply the energy of the hole. In this simple model, it is clear that for single acceptors the energy is lower when the magnetization is out of plane. In the limit that $\Delta \ll \xi$, $E_{\text{MAE}} \sim \frac{\Delta}{2}(1 - \frac{\Delta}{4\xi})$.

To determine the MAE using the VASP code⁸⁶, we adopt a two step procedure. We first perform a well-converged self-consistent spin-polarized calculation for the minimum energy geometry without SOC. The output from that calculation is used as input to the second step where SOC is added and the Kohn-Sham equation is solved non self-consistently yielding a new eigenvalue spectrum, Fermi energy and wavefunctions from which a total energy can be determined; to use the force theorem, we will just make use of the eigenvalue-sum part of the total-energy output. When adding the SOC, an orientation for the exchange field (magnetization direction) needs to be chosen and this will yield an orientation dependent eigenvalue spectrum, Fermi energy etc. To determine the MAE, we need to perform two calculations with the magnetization chosen (i) perpendicular to the plane and (ii) in plane. The MAE will be expressed as the difference. To calculate the single particle eigenvalue sum for the electronic structure shown in Fig. 19 requires a careful BZ summation^{81,83,87} for which we use the improved tetrahedron method.⁸⁸ The results obtained using the force theorem for a 6×6 supercell and 4, 8 and 12 divisions of the reciprocal lattice vectors are shown in Fig. 21 as a function of the BZ area element ($2s$) normalized to the area, S_{BZ} , of the BZ for a 1×1 primitive unit cell ($s \rightarrow 0$ for an infinite number of sampling k points and from the figure we expect a value of $\sim 0.8 \pm 0.2$ meV.

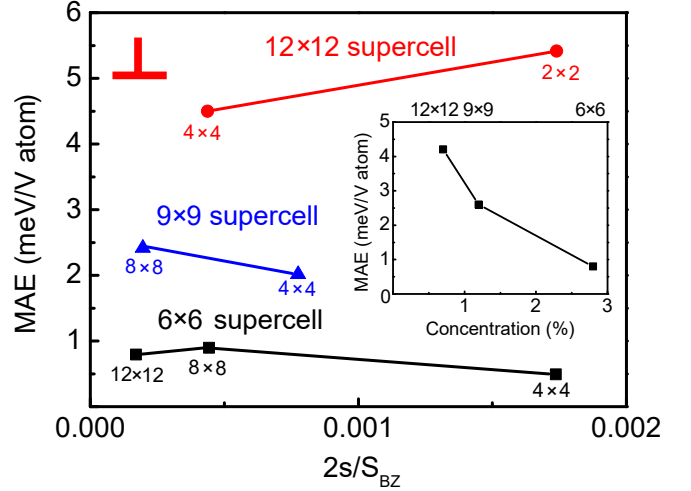


FIG. 21. (color online). Convergence of the anisotropy energy of a relaxed substitutional V_{Mo} atom in a monolayer of MoS_2 for 6×6 (black), 9×9 (blue) and 12×12 (red) supercells as a function of the area, s , of the triangular surface element used to perform the two-dimensional BZ integral, given as a fraction of the total area of the 2D BZ, S_{BZ} , for a 1×1 unit cell. The number of divisions of the reciprocal lattice vectors corresponding to each surface element is indicated for each supercell.

When the supercell size is increased and the dispersion of the e' and a'_1 states becomes smaller, we might expect the BZ summation to converge faster but the situation is complicated by the near-degeneracy of the e' and a'_1 bands. Fig. 21 includes results for 9×9 and 12×12 supercells indicating a strong increase in the size of the E_{MAE} in the single impurity limit. The strong dependence of the MAE on the supercell size can be understood in terms of the reduced dispersion of the impurity levels and the contribution to the MAE from states near the Fermi level whose degeneracy is lifted when the magnetization direction is rotated from in-plane with $\mathbf{M}\parallel a$ to out-of-plane with $\mathbf{M}\parallel c$ as illustrated by Fig. 19(d,e) and Fig. 20. For a 12×12 supercell, we can extrapolate the results obtained using a 2×2 and 4×4 k-point sampling to estimate a converged MAE of 4.2 meV. The exchange-splitting Δ is 15.2 meV for the e' level and using this value of Δ and $2\xi = 130$ meV in (15) yields a value of $E_{\text{MAE}} \sim 7.2$ meV that is still larger than the 4.2 meV estimate from the full calculation. We can extrapolate the results for the three sizes of supercell to $s = 0$ and then plot the results as a function of the inverse supercell size (inset) to estimate the SIA in the infinite supercell limit to be 4.5 ± 0.5 meV per V ion. This is much larger than the value reported for 2D CrI_3 ⁸⁹ that exhibits Ising behavior.¹¹ The dipole-dipole interactions that play an important role in determining whether or not the magnetization of thin magnetic layers and magnetic multilayers is in-plane or out-of-plane are orders of magnitude smaller in the present case and can be safely neglected.^{81,83,87}

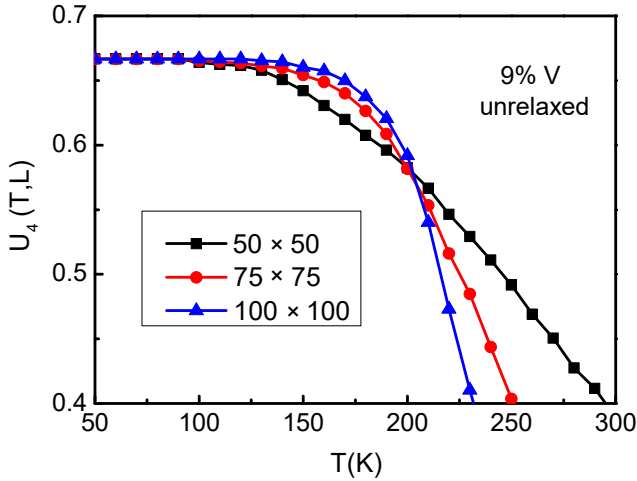


FIG. 22. Variation of the fourth order cumulant for three different supercell sizes $L = 50, 75, 100$ as a function of temperature.

B. Monte Carlo calculations

Very strong single-ion anisotropy combined with isotropic Heisenberg exchange results in Ising-like behaviour⁹⁰ which automatically gives a magnetically ordered phase at finite temperature.^{76,77} We map the energy differences calculated between FM and AFM oriented spins onto an isotropic Heisenberg exchange interaction and then model the V-doped MoS₂ monolayer as an Ising spin system for which all odd moments disappear in zero field by symmetry. Monte Carlo calculations are used to determine the Curie temperature T_C using Binder’s cumulant method^{91,92} where the fourth order cumulant of the magnetization \mathbf{M} simplifies to $U_4(T, L) = 1 - \langle M^4 \rangle / 3 \langle M^2 \rangle^2$. As the system size $L \rightarrow \infty$, $U_4 \rightarrow 0$ for $T > T_C$ and $U_4 \rightarrow 2/3$ for $T < T_C$. For large enough lattice size, $U_4(T, L)$ curves for different values of L cross as a function of temperature at a “fixed point” value U^* and the location of the crossing fixed point is the critical point.⁹²

At a given temperature and doping concentration, we establish thermodynamic equilibrium in 10^5 Monte Carlo (MC) thermalization steps and then average over 48 different random dopant configurations to obtain $\langle M^2 \rangle$ and $\langle M^4 \rangle$. Three different lattice sizes with $L = 50, 75, 100$ are used to calculate U_4 as a function of the temperature T with doping concentrations from 1% to 11%. An example of the results is shown in Fig. 22 where the fitting curve for the unrelaxed case in Fig. 12 is used to describe the exchange interactions for a doping concentration of 9%. The temperature corresponding to the size independent universal fixed point U^* where the $U_4(L, T)$ curves for different lattice sizes L intersect yields an estimate for T_C . For the largest supercell size $L = 100$, we calculated the magnetic susceptibility $\chi = [\langle M^2 \rangle - \langle |M| \rangle^2] / Nk_b T$ which diverges at the critical temperature in the ther-

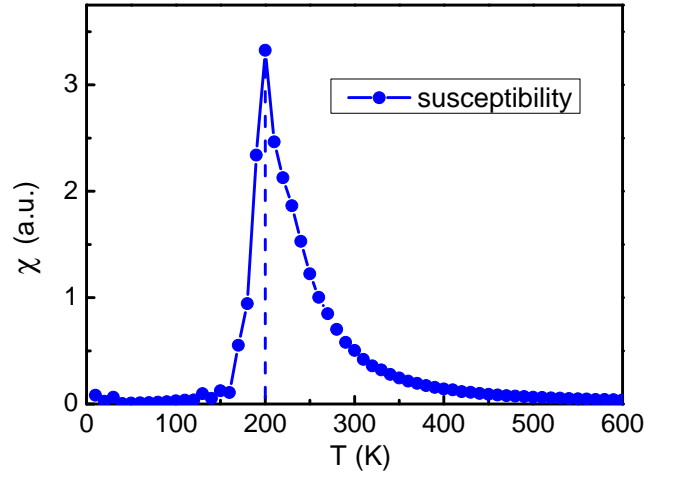


FIG. 23. Variation of the magnetic susceptibility as a function of temperature for 9% unrelaxed V dopant concentration with $L = 100$.

modynamic limit.⁹² An example is shown in Fig. 23 in which the Curie temperature obtained from the position of the magnetic susceptibility peak is in good agreement with that obtained from the fourth order cumulant.

C. Curie temperature

The ordering temperatures we calculate are shown in Fig. 24 for V doping concentrations x in the range from 1% to 11%. Without relaxation, $T_C(x)$ increases monotonically with doping concentration and reaches room

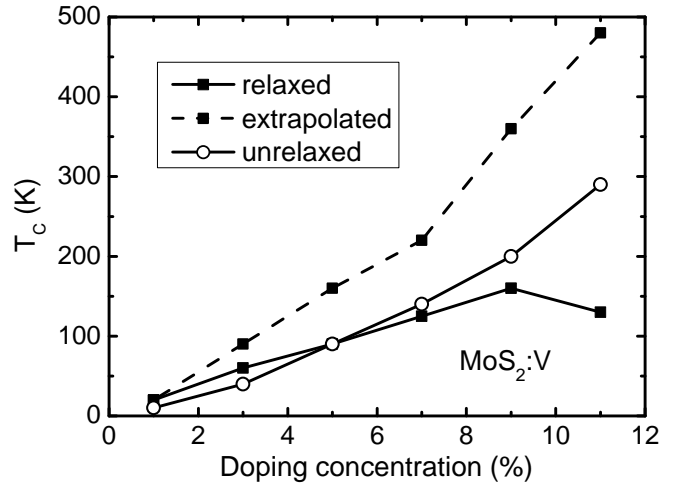


FIG. 24. Variation of the Curie temperature as a function of the doping concentration calculated using Binder’s cumulant method and the exchange interactions shown in Fig. 12 for an MoS₂ monolayer doped with V. The dashed curve was calculated by extrapolating the exchange interaction for relaxed dopant pairs to separations shorter than the critical separations where quenching occurs.

TABLE VII. Computational studies of single acceptor dopants in MoS₂. SC: Supercell. XC: Exchange-Correlation functional. MAE: Magnetic Anisotropy Energy. US-PP: Ultrasoft pseudopotential.⁹³ NC-PP: Norm-conserving pseudopotential.⁹⁴ PAW: Projector Augmented-Wave.⁵⁵ LDA: Local Density Approximation.⁶¹ CA: Ceperley-Alder.⁹⁵ GGA: Generalized Gradient Approximation. PBE: Perdew-Burke-Ernzerhof.⁶² HSE: Heyd-Scuseria-Ernzerhof.⁹⁶ QE: QUANTUM ESPRESSO.⁹⁷ VASP: Vienna Ab-initio Simulation Package.^{57,58} WIEN2K.⁹⁸ SIESTA.⁹⁹

SC size (# atoms)		Dopant	Method	XC	U(eV)	Vac. (Å)	Code	Exchange		Reference
Default	Max/test							MAE	Int. $J(d)$	
4 × 4		V, Nb, Ta	US-PP	GGA/PBE	0	10	QE	No	No	Cheng PRB13 ³⁵
4 × 4		V	PAW	GGA/PBE	0	12	VASP	No	No	Yue PLA13 ³⁶
5 × 5	6 × 6	Nb	NC-PP	LDA/CA	0	15	SIESTA	No	No	Dolui PRB13 ³³
		Nb	PAW	HSE	0		VASP	No	No	" "
5 × 5		V	PAW	GGA/PBE	0	15	VASP	No	No	Yun PCCP14 ³⁹
8 × 8		V	PAW	GGA/PBE	5.5		VASP	No	No	Andriotis PRB14 ⁴²
5 × 5	7 × 7	V, Nb, Ta	US-PP	GGA/PBE	0	12	QE	No	No	Lu NRL14 ²⁸
4 × 4		V	PAW	GGA/PBE	0	15	VASP	No	No	Miao JMS16 ⁴⁴
5 × 5		V	PAW	GGA/PBE	3	15	VASP	No	Yes	Fan NRL16 ⁴⁷
6 × 6		Cr, V	PAW	GGA/PBE	0	20	VASP	No	No	Robertson ACSN16 ⁴⁸
4 × 4	4 × 4	V, Cr	FLAPW	GGA	2.5	15	WIEN2K	No	No	Singh AM17 ⁴⁹
	8 × 5	V	PAW	GGA/PBE	0	16	VASP	No	Yes	Miao ASS18 ⁵⁰
6 × 6		Nb, Ta	PAW	HSE	0	17	VASP	No	No	Choi PRAP ¹⁰⁰
3 × 3	4 × 4	V	US-PP	GGA	3	20	QE	No	Yes	Mekonnen IJMPB18 ⁵¹
12 × 12	15 × 15	V, Nb, Ta	PAW	LDA(GGA)	—	20	VASP	Yes	Yes	This work

temperature for a concentration of $\sim 11\%$. With relaxation, the ferromagnetic exchange interaction is quenched for close dopant pairs and $T_C(x)$ exhibits a maximum of ~ 165 K for 9% doping. If we extrapolate the exchange interaction for relaxed dopant pairs to separations smaller than the critical separation where quenching occurs (dashed line in Fig. 12), the Curie temperature increases rapidly and monotonically with doping concentration and exceeds room temperature for dopant concentrations larger than 9%. Because the maximum value of $T_C(x)$ we obtain would be higher but for the quenching of the magnetic moments of closely separated relaxed dopants, it becomes important to consider how to suppress the quenching to obtain higher Curie temperatures. This will be discussed in Sec. VI.

V. COMPARISON WITH OTHER WORK

Table VII summarizes earlier computational work on doping MoS₂ monolayers with V, Nb or Ta. Because much of it was concerned with doping rather than with magnetic ordering, no attempts were made to calculate the magnetic anisotropy. Most of the calculations were done using small supercells and the separation dependence of the exchange interaction was not studied systematically, if at all. We noted in Sec. II that the GGA positions the Γ -point VBM too high with respect to the K-point VBM by comparison with experiment⁶⁰ and we therefore used the LDA that yields better agreement with experiment in this regard. Because most of the calculations referred to in Table VII were performed with the GGA exchange-correlation potential, we examine the effect of using the GGA rather than the LDA.

1. GGA versus LDA

If we use atomic configurations whose geometry was optimized using the LDA and repeat the electronic structure calculations using the GGA, we qualitatively reproduce the LDA results for the exchange interaction between V dopant atoms. The significant differences that will be documented below therefore have their origin in the only slightly different minimum-energy geometries predicted by the GGA.

Our starting point is an MoS₂ monolayer whose lattice

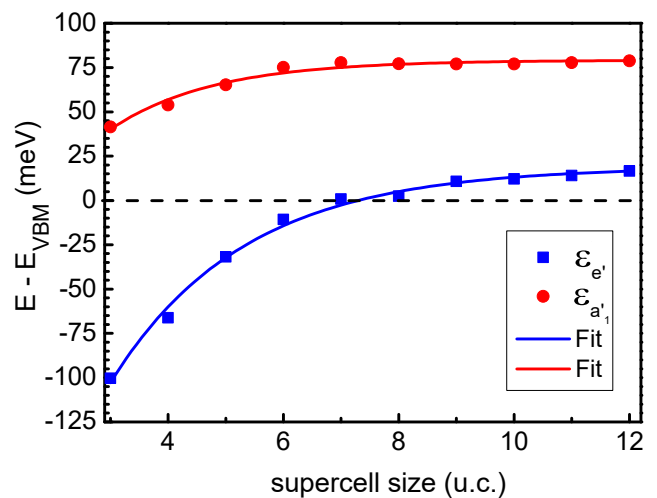


FIG. 25. Dependence on the supercell size N of the a_1' and e' impurity levels induced by an unrelaxed substitutional vanadium atom V_{Mo} with respect to the valence band maximum in the GGA.

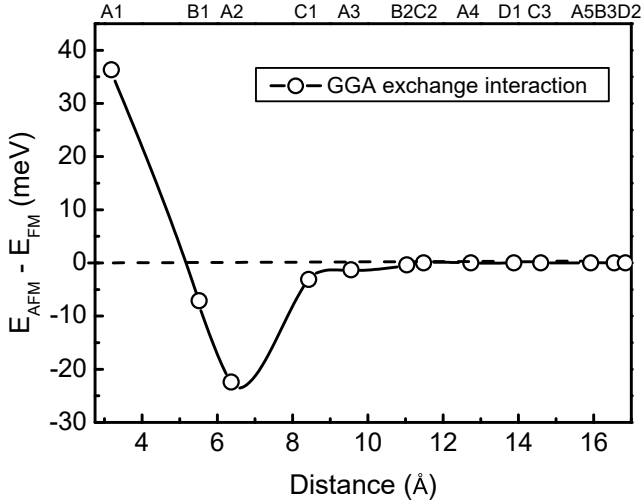


FIG. 26. The total energy difference between parallel and antiparallel aligned spins on the V dopants without relaxation within GGA.

constant $a_{\text{GGA}} = 3.185 \text{ \AA}$ minimizes the GGA total energy, Table I. The GGA overestimate of the position of the Γ -point VBM with respect to the K/K' VBM makes the a'_1 level much higher than the e' levels as shown in Fig. 25 where these levels are plotted as a function of supercell size. The asymptotic values are ~ 76 and ~ 20 meV for the a'_1 and e' states, respectively compared to ~ 62 meV for both in the LDA case, Fig. 7. Compared to the LDA estimate of a Bohr radius of 4.2 \AA from the radial extent of the partial charge density in Fig. 5, with the GGA we find a slightly larger value of 4.7 \AA for the a'_1 state. By analogy with a hydrogen atom where the extent of the $1s$ orbital increases greatly for the H^- ion compared to the neutral atom, we attribute the slightly larger radial extent for the more strongly bound hole in the GGA case to its greater a'_1 (hole) occupancy. In the GGA, the doped system is fully spin-polarized for the smallest 3×3 supercell we considered and the a'_1 exchange splitting of 142 meV is much larger than the 91 meV we found in the unrelaxed LDA case. (The LDA predicts an exchange splitting of $\Delta\varepsilon_{1s} = \varepsilon_{1s}^\uparrow - \varepsilon_{1s}^\downarrow = 0.35$ Rydberg for a hydrogen atom compared to 0.55 Rydberg for the GGA; see appendix B).

Fig. 26 shows the exchange interaction calculated with the GGA for pairs of unrelaxed V_{Mo} dopants as a function of the distance between them. We observe an oscillatory behavior with FM coupling for neighbouring pairs (“A1” configuration, see Fig. 3) that switches to AFM for B1, A2, C1 and A3 configurations after which it is essentially zero reflecting the small effective Bohr radius of the a'_1 level ($a_0^* \sim 4.7 \text{ \AA}$). The relatively large separation in energy of the a'_1 and e' levels means that for separations larger than $\sim 9 \text{ \AA}$, both holes are to be found in the anti-bonding a^* level because the bonding-antibonding interaction is too weak to lead to hole occupancy of the e^* level. Because both holes must of necessity occupy the

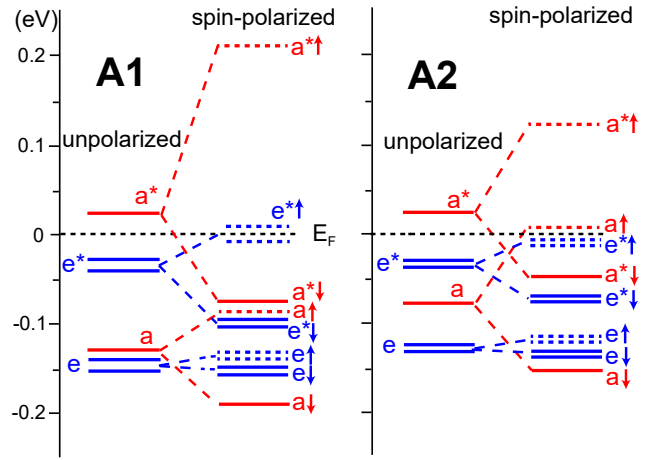


FIG. 27. Energy diagrams for unrelaxed dopant pairs in A1 and A2 configurations (Fig. 3) with and without spin polarization calculated in GGA. The levels are calculated from the appropriate weighted average of the Γ , K/K' and M eigenvalues as in figures 13 and 16. The Fermi level is indicated as a black dashed horizontal line. The spin up and spin down states are represented as dashed and solid lines, respectively.

a^* level, their spins must be opposite and FM ordering is energetically unfavourable (though the energy difference is very small).

To understand the oscillation for small separations, we consider the electronic structures of the a'_1 and e' derived a - a^* and e - e^* bonding and antibonding states for the A1 and A2 configurations in Fig. 27 with and without spin polarization. We begin with the A1 configuration. Compared to the LDA case that was shown in Fig. 13(b), we see that the unpolarized a and a^* levels (lhs of Fig. 27) are higher than the e - e^* levels reflecting the corresponding feature for a single substitutional dopant and that the a - a^* bonding-antibonding interaction is larger because the Bohr radius of the a'_1 states is larger in the GGA. On the rhs of the A1 panel, we see that the exchange splitting of the a^* levels is approximately doubled to ~ 300 meV for the A1 configuration compared to the single V_{Mo} case because of the overlapping hole densities; the same doubling occurs in the LSDA, where the exchange splitting of 92 meV for a single substitutional V is enhanced to 180 meV for neighbouring V pairs, see Fig. 15. The exchange splitting is so large that the down-spin a^* level moves below the (approximately doubly) degenerate up-spin e^* level with the result that the hole can flip its spin and the Fermi level is pinned in the half-filled up-spin e^* state. By having one hole in an a^* state and the other in an e^* state it is possible for their spins to be parallel and to simultaneously gain spin-polarization and bonding energy.

As the separation between the V_{Mo} atoms is increased, the exchange splitting and bonding interaction decrease rapidly for the a states and a FM triplet state is only formed at the expense of having one hole oc-

cupying a bonding a state (rhs of A2 panel); spin-polarization energy gain is offset by loss of bonding energy. Antiparallel alignment of the holes allowing gain of both spin-polarization and bonding energy becomes more favourable.

The effect of relaxation is to push the a'_1 level up in energy and increase the a - a^* bonding-antibonding splitting so that the unpolarized electronic structure resembles that of Fig. 13(e) with both holes in the a^* level. For dopant separations less than ~ 10 Å this leads to quenching of the magnetism. For separations larger than this, the a'_1 levels ($a_0^* \sim 4.7$ Å) interact only weakly with each other leading to very small energy differences $E_{\text{AFM}} - E_{\text{FM}}$ and negligible exchange interaction because the e' related levels are too low in energy to be occupied.

As anticipated at the beginning of this section, we can trace the large difference between the GGA and LDA descriptions of the exchange interaction between pairs of V_{Mo} dopants to the 2% difference between the LDA and GGA lattice constants. If we use the experimental lattice parameters listed in Table I, the differences between LDA and GGA disappear and we find that near-degenerate e' and a'_1 impurity levels with binding energies of 56 meV in a direct band gap of 1.78 eV couple ferromagnetically for all separations. The different orbital character of the e' and a'_1 levels means that they are very sensitive to the in-plane lattice constant a and out-of-plane d_{SS} , respectively, whose ratio determines their relative positions. From Table I, we see that the LDA ratio of 1.001 is much closer to the experimental value of 0.996 than the GGA ratio of 1.018 and argue that the LDA provides a more reasonable description of the relative position of the impurity levels.

When SOC is taken into consideration, the energy difference $\Delta_{\text{K}\Gamma}$ between the K/K' and Γ -point valence band maxima increases from 150 to 216 meV for LDA and from 12 to 88 meV for GGA, respectively, because of the large spin-orbit splitting at the K/K' point, Table VIII. The experimental value, 140 meV, is just in between making it unclear what will actually happen. To resolve this issue, experiment should focus on determining the position of the a'_1 level with respect to the top of the valence band in the single impurity limit.

Because the relative position of the impurity states determines the exchange interaction between dopant atoms, we have performed exploratory calculations to tune the relative positions of the K/K' and Γ valence band maxima and consequently of the a'_1 and e' levels with strain. For GGA, a 1% compressive strain ($\Delta a < 0$) is found to lower the a'_1 levels to be degenerate with the e' levels and we find FM coupling for all separations. 2% tensile strain ($\Delta a > 0$) lifts the a'_1 levels far above the e' levels stabilizing the magnetic moment of single impurities but favouring singlet formation of impurity pairs and AFM coupling. So while tensile strain reduces the formation energies of Nb_{Mo} and Ta_{Mo} and facilitates p doping of MoS_2 ,¹⁰⁰ it is detrimental for ferromagnetic ordering.

If the exchange interactions are so sensitive to the lat-

TABLE VIII. Effect of SOC on the band gap $\Delta\varepsilon_g$ and valence band alignment for an MoS_2 monolayer in the LDA and GGA. $\Delta_{\text{K}\Gamma} = \varepsilon_{\text{K}} - \varepsilon_{\Gamma}$ is the energy difference between the valence band maximum (VBM) at the K and Γ points.

	No SOC		Including SOC	
	$\Delta\varepsilon_g$ (eV)	$\Delta_{\text{K}\Gamma}$	$\Delta\varepsilon_g$ (eV)	$\Delta_{\text{K}\Gamma}$
GGA	1.650	0.012	1.586	0.088
LDA	1.860	0.150	1.787	0.216
Exp			1.900 ^a	0.140 ^b

^aRef.17 ^bRef.60

tice constant and the ratio of a to d_{SS} , it might be useful to consider tuning this ratio by modifying $\Delta_{\text{K}\Gamma}$ either using strain or by alloying, $\text{Mo}(\text{S}/\text{Se}/\text{Te})_2$. In the MoSe_2 , MoTe_2 and WSe_2 systems, the a'_1 level lies so much lower than the e' level that using GGA or LDA with their different lattice parameters has little effect; the coupling is dominated by the long range of the e' levels.

2. LDA + U

Two of the studies cited in Table VII use a finite value of U to better describe onsite Coulomb repulsion between electrons in localized d orbitals.^{42,49} We find that LDA+U⁷⁴ with modest values of U makes the local magnetic moment more localized and enhances it. The (more localized) a'_1 level is more sensitive to U than the e' level.

A small value of U (less than 1 eV) increases the exchange splitting of the a'_1 level and increases the FM exchange interaction which would yield a larger T_{C} compared to calculations without U . A larger value of U (larger than 3 eV) causes the hole to become even more localized and fully polarized even at very high concentrations (25%). As a consequence, the exchange interaction decays more rapidly and the separation below which quenching occurs decreases because the bonding interaction decays more rapidly. Compared to LDA calculations, the Curie temperature would be lower at low dopant concentration but enhanced at high concentration.

In our LDA calculations, we find that the shallow vanadium $3d$ orbitals hybridize strongly with S- $3p$ and Mo- $4d$ orbitals delocalizing the holes. We expect the Coulomb U in our system to be small and with a small U , the Curie temperature should be enhanced. Our LDA results should thus represent a lower bound on the exchange interaction and ordering temperature.

VI. DISCUSSION

According to the Zener p - d model used to interpret magnetic coupling in $\text{Ga}(\text{Mn})\text{As}$ dilute magnetic semiconductors,⁴ holes in As (p) bonding states mediate the exchange interaction between strong local (d^5) mag-

netic moments on Mn^{2+} dopant ions. In the present case, the magnetic moments that we find come from unpaired (d^1) spins in gap states that are only weakly bound by the Coulomb potential of the dopant ions, Fig. 2. The large Bohr radii we find for these states, Table II, allows them to overlap to form narrow bands and suggests that on-site Coulomb interactions may play a minor role and a model of itinerant ferromagnetism may be more appropriate than the various localized models used to study the Ga(Mn)As and related systems.^{5,6} When the holes are in orbitally nondegenerate a'_1 levels, AFM coupling is favoured to satisfy Pauli's exclusion principle; when they are in the degenerate e' levels, FM coupling is preferred to minimize the Coulomb interaction. For MoS_2 , the (accidental) near-degeneracy of the a'_1 and e' hole states leads to them competing to determine the magnetic properties whereby the strength of the exchange interaction is related to the exchange splitting of the impurity band and will be affected by the band dispersion for high doping concentrations.

In the low doping limit, the impurity states have no dispersion and are fully polarized. As the impurity concentration is increased, the impurity levels overlap to form narrow bands that broaden and eventually overlap the narrow Mo band that forms the top of the valence band. As seen in Fig. 8, the impurity bandwidth increases exponentially with increasing doping concentration. For the 9% V dopant concentration for which we find T_C to be a maximum, the e' impurity bandwidth is ~ 400 meV. The a'_1 band is narrower, only about a third as wide. Both bandwidths exceed the 91 meV exchange splitting we find for single V impurities in Fig. 10 that would imply partial quenching of the magnetic moments. For the ordered V dopants studied in Table IV, this quenching occurs as the concentration is increased above 3% and is complete by 6%. For itinerant electrons occupying narrow bands, it has been argued that the effective interaction predicted by the Stoner criterion will not be reduced by correlation effects or spin wave excitations.⁵⁴ In contrast to traditional dilute magnetic semiconductors with large local moments that do not contribute to the spin stiffness, the completely spin polarized carriers in narrow impurity bands lead to a large spin stiffness and develop ferromagnetic ordering by their mutual interaction.

The quenching of ferromagnetic pairing for close impurity pairs can be avoided by considering instead of MoS_2 as host semiconductor, MoSe_2 or MoTe_2 (WSe_2 or WTe_2) for which the Γ point VBM drops with respect to the K/K' VBM as $\text{S} \rightarrow \text{Se} \rightarrow \text{Te}$ (sketched in Fig. 28). Preliminary calculations show that the a'_1 defect levels do indeed follow the Γ point VBM leaving the holes in the orbitally degenerate e' derived impurity bands. The increased lattice constant makes the e' states more localized and enhances the spin polarization in MoSe_2 and MoTe_2 . Very recently there have been reports of long-range and/or room temperature ferromagnetism occurring in V doped WSe_2 monolayers,¹⁰¹ in MoSe_2 and MoTe_2 ,¹⁰² in V and Ta doped MoTe_2 ^{103,104} and in MoS_2 ¹⁰⁵ whereby the in-

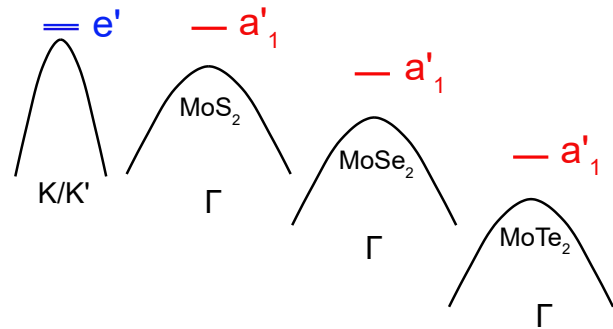


FIG. 28. Schematic of the relative position of VBM at K and Gamma points and corresponding impurity levels for MX₂.

teraction with anion vacancies would appear to play an important role. These systems clearly warrant closer study.

We might expect double acceptors to have larger magnetic moments and exchange interactions. However, when MoS_2 is doped with Ti, Zr, Hf on the Mo site, the a'_1 level is lifted far above the e' levels and accommodates both holes so such substitutional impurities are nonmagnetic in the single impurity limit. Only when dopant pairs are sufficiently close (~ 6 Å) does strong π bonding lift the e^* antibonding level above the a bonding level so all four holes occupy antibonding states. The two holes in the e^* states can become ferromagnetic with a total magnetic moment of $2 \mu_B$ but this does not represent an improvement on the single acceptor case.

In MoSe_2 or MoTe_2 (WSe_2 or WTe_2) monolayers where the Γ point VBM lies well below the K/K' VBM, the two holes introduced by double acceptors occupy e' states that can accommodate four holes. Half-filling of these degenerate levels leads to a competition between Jahn-Teller distortion and exchange splitting. If the Jahn-Teller distortion is sufficiently strong, the magnetic moment will be quenched and we do not expect double acceptors to be magnetic for low doping concentrations.

VII. SUMMARY & CONCLUSIONS

We have used *ab initio* calculations to explore the possibility of inducing ferromagnetism in an MoS_2 monolayer by substitutionally doping it with V, Nb or Ta on Mo sites. In the single impurity limit, the resulting repulsive Coulomb potential leads to a doubly degenerate $\{d_{xy}, d_{x^2-y^2}\}$ state with e' symmetry bound to the K/K' valence band maxima and a singly degenerate a'_1 state with $d_{3z^2-r^2}$ character bound to the slightly lower-lying Γ -point valence band maximum that are accidentally degenerate. The exchange interaction between two such hole states depends on whether the holes have a'_1 or e' character, the former being quite localized, the latter quite extended in space. The magnetic moments of the

spin $\frac{1}{2}$ acceptor states couple ferromagnetically at low concentrations but if the dopants are closer than the effective Bohr radius of the $d_{3z^2-r^2}$ orbital, the magnetic moments quench in order to profit from the bonding interaction. The details of the exchange interaction depend sensitively on the equilibrium structure of the undoped monolayer that in turn depends on the (approximate) exchange-correlation functional used. We argue that the LDA is preferable to the GGA because it describes the ordering of the K/K' and Γ valence band maxima better compared to experiment.

When spin-orbit coupling is included, we calculate a large magnetic anisotropy energy for acceptors with a preference for out of plane orientation and argue that this large single ion anisotropy justifies using an Ising spin model to study the ferromagnetic ordering. We estimate the ordering temperature by combining our (isotropic) separation-dependent exchange interactions with Monte Carlo calculations using Binder's cumulant method. For an MoS₂ monolayer doped with V (Nb or Ta), we estimate ferromagnetic Curie temperatures as a function of the dopant concentration and find a maximum T_C of ~ 170 K (~ 100 K) at around 9% dopant concentration. At sufficiently high concentrations of impurity states, the acceptor states form bands and magnetism is quenched when the bandwidth exceeds a critical value; this critical value depends sensitively on the exchange-correlation functional used.

Although the maximum calculated T_C is below room temperature, our work demonstrates that shallow impurities in MX₂ monolayers that bind weakly but have long range interactions are promising dopants to explore with a view to realizing room temperature ferromagnetism.

ACKNOWLEDGMENTS

This work was financially supported by the “Nederlandse Organisatie voor Wetenschappelijk Onderzoek” (NWO) through the research programme of the former “Stichting voor Fundamenteel Onderzoek der Materie,” (NWO-I, formerly FOM) and through the use of supercomputer facilities of NWO “Exacte Wetenschappen” (Physical Sciences). Y. G. thanks the China Scholarship Council for financial support. N.G. is grateful to Dr. Supravat Dey for fruitful discussions.

Appendix A: Sulphur reference atom

The impurity potential of a vanadium acceptor screened by a hole in the a_1' and e' states as felt by S atoms is plotted in the insets to Fig. 29. The effective Bohr radii of these impurity states determined by fitting to Eq. (1b) are 8.8 Å for screening by the e' state and 6.5 Å for screening by the a_1' state. For the e' level, this effective Bohr radius is consistent with the other estimates summarized in Table II. For the a_1' level, however,

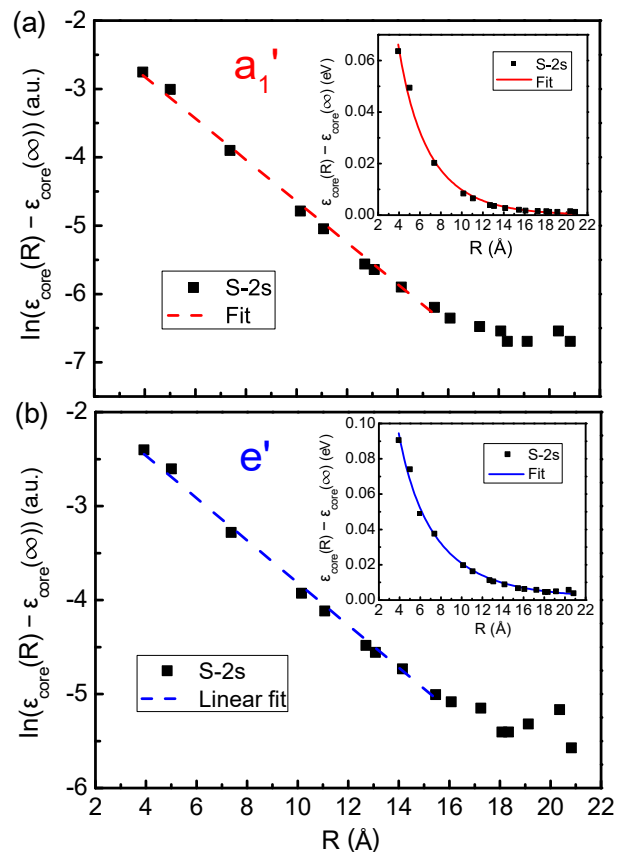


FIG. 29. Dependence of the S 2s semicore levels on the separation from the V_{Mo} dopant ion. The (screened) Coulomb potential of the V dopant is screened by the a_1' hole (upper panel) respectively by the e' hole (lower panel). The asymptotic value $\epsilon_{\text{core}}(\infty)$ was determined by fitting the calculated data points in the insets to an exponential wave function and using this fit (red curves) to extrapolate to $R = \infty$.

the value of 6.5 Å yielded by the S atom probes is larger than the value of 5.4 Å yielded by using Mo atoms as probes. We already saw more scatter in the estimate of the a_1' radius and in view of its very small value and the importance of the central cell potential and local screening effects on this length scale, it is not surprising to see this type of variation measured by probes at different radial distances.

Appendix B: Hydrogen atom in LDA/GGA

In the local density approximation (LDA), the total energy of a neutral hydrogen atom is not -1 Rydberg but its absolute value is about 10% smaller, ~ -0.89 Rydberg and the Kohn-Sham eigenvalue for the $1s$ state is $\epsilon_{1s} = -0.46$.⁶⁷ It has been shown that the discrepancy can be substantially reduced by using the spin-polarized (SP) version of the LDA, the local spin density approximation (LSDA).⁶⁷ Using the Perdew-Zunger⁶¹ parameterization of L(S)DA, we obtain total energies (E) and

TABLE IX. Comparison of total energies (E) and Kohn-Sham (KS) eigenvalues (ε) for a hydrogen atom as described by the LDA and the LSDA, the non-spin polarized (NSP)-GGA and spin-polarized (SP)-GGA in Rydberg units (13.606 eV).

	LDA		GGA	
	NSP	SP	NSP	SP
E	-0.89	-0.97	-0.92	-0.99
$\varepsilon_{1s}^{\uparrow}$	-0.46	-0.18	-0.47	0.00
$\varepsilon_{1s}^{\downarrow}$	-0.46	-0.53	-0.47	-0.55
$\Delta\varepsilon_{1s}$	0.00	0.35	0.00	0.55

KS eigenvalues (ε) of $E = -0.89$ Ry, $\varepsilon = -0.46$ Ry (LDA) and $E = -0.97$ Ry (LSDA) and an exchange splitting of the Kohn-Sham $1s$ eigenvalues of -0.35 Ry. If instead of the L(S)DA, we use the Perdew-Burke-Ernzerhof⁶² GGA, we obtain energies of -0.92 Ry (GGA) and -0.99 Ry (SP-GGA) and an exchange splitting of -0.55 Ry.

* Email: Y.Gao@utwente.nl

† Email: nganguli@iiserb.ac.in; Present address: Department of Physics, Indian Institute of Science Education and Research Bhopal, Bhauri, Bhopal 462066, India

‡ Email: P.J.Kelly@utwente.nl

- ¹ H. Ohno, H. Munekata, T. Penney, S. von Molnár, and L. L. Chang, “Magnetotransport properties of p -type (In,Mn)As diluted magnetic III-V semiconductors,” *Phys. Rev. Lett.* **68**, 2664–2667 (1992).
- ² H. Ohno, A. Shen, F. Matsukura, A. Oiwa, A. Endo, S. Katsumoto, and Y. Iye, “(Ga,Mn)As: A new diluted magnetic semiconductor based on GaAs,” *Appl. Phys. Lett.* **69**, 363–365 (1996).
- ³ T. Dietl, H. Ohno, F. Matsukura, J. Cibert, and D. Ferrand, “Zener model description of ferromagnetism in zincblende magnetic semiconductors,” *Science* **287**, 1019–1022 (2000).
- ⁴ Tomasz Dietl, “A ten-year perspective on dilute magnetic semiconductors and oxides,” *Nat. Mater.* **9**, 965–974 (2010).
- ⁵ T. Jungwirth, Jairo Sinova, J. Mašek, J. Kučera, and A. H. MacDonald, “Theory of ferromagnetic (III,Mn)V semiconductors,” *Rev. Mod. Phys.* **78**, 809–864 (2006).
- ⁶ K. Sato, L. Bergqvist, J. Kudrnovský, P. H. Dederichs, O. Eriksson, I. Turek, B. Sanyal, G. Bouzerar, H. Katayama-Yoshida, V. A. Dinh, T. Fukushima, H. Kizaki, and R. Zeller, “First-principles theory of dilute magnetic semiconductors,” *Rev. Mod. Phys.* **82**, 1633–1690 (2010).
- ⁷ N. D. Mermin and H. Wagner, “Absence of Ferromagnetism or Antiferromagnetism in One- or Two-Dimensional Isotropic Heisenberg Models,” *Phys. Rev. Lett.* **17**, 1133–1136 (1966).
- ⁸ P. C. Hohenberg, “Existence of long-range order in one and two dimensions,” *Phys. Rev.* **158**, 383–386 (1967).
- ⁹ in *Ultrathin Magnetic Structures I-IV*, edited by J. A. C. Bland and B. Heinrich (Springer-Verlag, Berlin, 1994–2005).
- ¹⁰ Cheng Gong, Lin Li, Zhenglu Li, Huiwen Ji, Alex Stern, Yang Xia, Ting Cao, Wei Bao, Chenzhe Wang, Yuan Wang, Z. Q. Qiu, R. J. Cava, Steven G. Louie, Jing Xia, and Xiang Zhang, “Discovery of intrinsic ferromagnetism in two-dimensional van der Waals crystals,” *Nature (London)* **546**, 265–269 (2017).
- ¹¹ Bevin Huang, Genevieve Clark, Efrén Navarro-Moratalla, Dahlia R. Klein, Ran Cheng, Kyle L. Seyler, Ding Zhong, Emma Schmidgall, Michael A. McGuire, David H. Cob-

den, Wang Yao, Di Xiao, Pablo Jarillo-Herrero, and Xiaodong Xu, “Layer-dependent ferromagnetism in a van der Waals crystal down to the monolayer limit,” *Nature (London)* **546**, 270–273 (2017).

- ¹² Nitin Samarth, “Magnetism in flatland,” *Nature (London)* **546**, 216–218 (2017).
- ¹³ K. S. Novoselov, A. K. Geim, S. V. Morozov, D. Jiang, Y. Zhang, S. V. Dubonos, I. V. Grigorieva, and A. A. Firsov, “Electric Field Effect in Atomically Thin Carbon Films,” *Science* **306**, 666–669 (2004).
- ¹⁴ K. S. Novoselov, D. Jiang, F. Schedin, T. J. Booth, V. V. Khotkevich, S. V. Morozov, and A. K. Geim, “Two-dimensional atomic crystals,” *Proc. Natl. Acad. Sci. U.S.A.* **102**, 10451–10453 (2005).
- ¹⁵ K. S. Novoselov, V. I. Fal’ko, L. Colombo, P. R. Gellert, M. G. Schwab, and K. Kim, “A roadmap for graphene,” *Nature (London)* **490**, 192–200 (2012).
- ¹⁶ Andrea Splendiani, Liang Sun, Yuanbo Zhang, Tianshu Li, Jonghwan Kim, Chi-Yung Chim, Giulia Galli, and Feng Wang, “Emerging photoluminescence in monolayer MoS₂,” *Nano Letters* **10**, 1271–1275 (2010).
- ¹⁷ Kin Fai Mak, Changgu Lee, James Hone, Jie Shan, and Tony F. Heinz, “Atomically Thin MoS₂: A New Direct-Gap Semiconductor,” *Phys. Rev. Lett.* **105**, 136805 (2010).
- ¹⁸ B. Radisavljevic, A. Radenovic, J. Brivio, V. Giacometti, and A. Kis, “Single-layer MoS₂ transistors,” *Nat. Nanotechnol.* **6**, 147–150 (2011).
- ¹⁹ A. K. Geim and I. V. Grigorieva, “Van der Waals heterostructures,” *Nature (London)* **499**, 419–425 (2013).
- ²⁰ M. Gibertini, M. Koperski, A. F. Morpurgo, and K. S. Novoselov, “Magnetic 2D materials and heterostructures,” *Nat. Nanotechnol.* **14**, 408–419 (2019).
- ²¹ Manuel Bonilla, Sadhu Kolekar, Yujing Ma, H. C. Diaz, Vijaysankar Kalappattil, Raja Das, Tatiana Eggers, H. R. Gutierrez, Manh-Huong Phan, and Matthias Batzill, “Strong room-temperature ferromagnetism in VSe₂ monolayers on van der Waals substrates,” *Nat. Nanotechnol.* **13**, 289–294 (2018).
- ²² Yujun Deng, Yijun Yu, Yichen Song, Jingzhao Zhang, Nai Zhou Wang, Zeyuan Sun, Yangfan Yi, Yi Zheng Wu, Shiwei Wu, Junyi Zhu, Jing Wang, Xian Hui Chen, and Yuanbo Zhang, “Gate-tunable room-temperature ferromagnetism in two-dimensional Fe₃GeTe₂,” *Nature (London)* **563**, 94–99 (2018).
- ²³ Though they state that they are studying trigonal prismatic (H) monolayers, it is clear from their sketches of

- the structure as well as the density of states and magnetic moments that the calculations of Ma *et al.* were for the octahedral (T) phase.¹⁰⁶ Subsequent studies of both phases^{107–112} find the H phase to have a lower energy and to be magnetic with a moment of $1\mu_B/V$ atom.
- ²⁴ T. Li and G. Galli, “Electronic properties of MoS₂ nanoparticles,” *J. Phys. Chem. C* **111**, 16192–16196 (2007).
 - ²⁵ R. A. Bromley, R. B. Murray, and A. D. Yoffe, “The band structures of some transition metal dichalcogenides: III. Group VI A: trigonal prism materials,” *J. Phys. C: Sol. State Phys.* **5**, 759–778 (1972).
 - ²⁶ L. F. Mattheiss, “Band structures of transition-metal-dichalcogenide layer compounds,” *Phys. Rev. B* **8**, 3719–3740 (1973).
 - ²⁷ C. Ataca and S. Ciraci, “Functionalization of single-layer MoS₂ honeycomb structures,” *J. Phys. Chem. C* **115**, 13303–13311 (2011).
 - ²⁸ Shang-Chun Lu and Jean-Pierre Leburton, “Electronic structures of defects and magnetic impurities in MoS₂ monolayers,” *Nanoscale Research Letters* **9**, 676 (2014).
 - ²⁹ Jinhua Hong, Zhixin Hu, Matt Probert, Kun Li, Danhui Lv, Xinan Yang, Lin Gu, Nannan Mao, Qingliang Feng, Liming Xie, Jin Zhang, Dianzhong Wu, Zhiyong Zhang, Chuanhong Jin, Wei Ji, Xixiang Zhang, Jun Yuan, and Ze Zhang, “Exploring atomic defects in molybdenum disulphide monolayers,” *Nat. Communications* **6**, 6293 (2015).
 - ³⁰ Wun-Fan Li, Changming Fang, and Marijn A. van Huis, “Strong spin-orbit splitting and magnetism of point defect states in monolayer WS₂,” *Phys. Rev. B* **94**, 195425 (2016).
 - ³¹ M. A. Khan and Michael N. Leuenberger, “Room-temperature superparamagnetism due to giant magnetic anisotropy in MoS₅ defected single-layer MoS₂,” *J. Phys.: Condens. Matter* **30**, 155802 (2018).
 - ³² Jiangang He, Kechen Wu, Rongjian Sa, Qiaohong Li, and Yongqin Wei, “Magnetic properties of nonmetal atoms absorbed MoS₂ monolayers,” *Appl. Phys. Lett.* **96**, 082504 (2010).
 - ³³ Kapildeb Dolui, Ivan Rungger, Chaitanya Das Pemasaraju, and Stefano Sanvito, “Possible doping strategies for MoS₂ monolayers: An *ab initio* study,” *Phys. Rev. B* **88**, 075420 (2013).
 - ³⁴ J. Karthikeyan, H. P. Komsa, M. Batzill, and A. V. Krasheninnikov, “Which transition metal atoms can be embedded into two-dimensional molybdenum dichalcogenides and add magnetism?” *Nano Letters* **19**, 4581–4587 (2019).
 - ³⁵ Y. C. Cheng, Z. Y. Zhu, W. B. Mi, Z. B. Guo, and U. Schwingenschlöggl, “Prediction of two-dimensional diluted magnetic semiconductors: Doped monolayer MoS₂ systems,” *Phys. Rev. B* **87**, 100401(R) (2013).
 - ³⁶ Qu Yue, Shengli Chang, Shiqiao Qin, and Jingbo Li, “Functionalization of monolayer MoS₂ by substitutional doping: A first-principles study,” *Phys. Lett. A* **377**, 1362–1367 (2013).
 - ³⁷ Ashwin Ramasubramaniam and Doron Naveh, “Mn-doped monolayer MoS₂: An atomically thin dilute magnetic semiconductor,” *Phys. Rev. B* **87**, 195201 (2013).
 - ³⁸ Rohan Mishra, Wu Zhou, Stephen J. Pennycook, Sokrates T. Pantelides, and Juan-Carlos Idrobo, “Long-range ferromagnetic ordering in manganese-doped two-dimensional dichalcogenides,” *Phys. Rev. B* **88**, 144409 (2013).
 - ³⁹ Won Seok Yun and J. D. Lee, “Unexpected strong magnetism of Cu doped single-layer MoS₂ and its origin,” *Physical Chemistry Chemical Physics* **16**, 8990–8996 (2014).
 - ⁴⁰ Jingshan Qi, Xiao Li, Xiaofang Chen, and Kaige Hu, “Strain tuning of magnetism in Mn doped MoS₂ monolayer,” *J. Phys.: Condens. Matter* **26**, 256003 (2014).
 - ⁴¹ Carmen J. Gil, Anh Pham, Aibing Yu, and Sean Li, “An *ab initio* study of transition metals doped with WSe₂ for long-range room temperature ferromagnetism in two-dimensional transition metal dichalcogenide,” *J. Phys.: Condens. Matter* **26**, 306004 (2014).
 - ⁴² Antonis N. Andriotis and Madhu Menon, “Tunable magnetic properties of transition metal doped MoS₂,” *Phys. Rev. B* **90**, 125304 (2014).
 - ⁴³ Jianmin Zhang, Huiling Zheng, Ruilin Han, Xiaobo Du, and Yu Yan, “Tuning magnetic properties of CrS₂ monolayer by doping transition metal and alkaline-earth atoms,” *J. Alloys Compd.* **647**, 75–81 (2015).
 - ⁴⁴ Yaping Miao, Yuhong Huang, Qinglong Fang, Zhi Yang, Kewei Xu, Fei Ma, and Paul K. Chu, “Tuning of electronic states and magnetic polarization in monolayered MoS₂ by codoping with transition metals and nonmetals,” *J. Mater. Sci.* **51**, 9514–9525 (2016).
 - ⁴⁵ Xu Zhao, Congxin Xia, Tianxing Wang, and Xianqi Dai, “Electronic and magnetic properties of X-doped (X = Ti, Zr, Hf) tungsten disulphide monolayer,” *J. Alloys Compd.* **654**, 574–579 (2016).
 - ⁴⁶ Xu Zhao, Peng Chen, Congxin Xia, Tianxing Wang, and Xianqi Dai, “Electronic and magnetic properties of *n*-type and *p*-doped MoS₂ monolayers,” *RSC Advances* **6**, 16772 (2016).
 - ⁴⁷ Xiao-Li Fan, Yu-Rong An, and Wen-Jun Guo, “Ferromagnetism in transitional metal-doped MoS₂ monolayer,” *Nanoscale Research Letters* **11**, 154 (2016).
 - ⁴⁸ Alex W. Robertson, Yung-Chang Lin, Shanshan Wang, Hidetaka Sawada, Christopher S. Allen, Qu Chen, Sungwoo Lee, Gun-Do Lee, Joohee Lee, Seungwu Han, Euijoon Yoon, Angus I. Kirkland, Heeyeon Kim, Kazu Sue-naga, and Jamie H. Warner, “Atomic structure and spectroscopy of single metal (Cr, V) substitutional dopants in monolayer MoS₂,” *ACS Nano* **10**, 10227–10236 (2016).
 - ⁴⁹ N. Singh and U. Schwingenschlöggl, “A route to permanent valley polarization in monolayer MoS₂,” *Adv. Mater.* **29**, 1600970 (2017).
 - ⁵⁰ Yaping Miao, Yan Li, Qinglong Fang, Yuhong Huang, Yunjin Sund, Kewei Xub, Fei Ma, and Paul K. Chu, “Effects of dopant separation on electronic states and magnetism in monolayer MoS₂,” *Appl. Surf. Sci.* **428**, 226–232 (2018).
 - ⁵¹ Sintayehu Mekonnen and Pooran Singh, “Electronic structure and nearly room-temperature ferromagnetism in V-doped monolayer and bilayer MoS₂,” *International Journal of Modern Physics B* **32**, 1850231 (2018).
 - ⁵² A short summary of this work appeared in Yuqiang Gao, Nirmal Ganguli, and Paul J. Kelly, “Itinerant ferromagnetism in *p*-doped monolayers of MoS₂,” *Phys. Rev. B* **99**, 220406(R) (2019).
 - ⁵³ Hartwin Peelaers and Chris G. Van de Walle, “Effects of strain on band structure and effective masses in MoS₂,” *Phys. Rev. B* **86**, 241401 (2012).
 - ⁵⁴ D. M. Edwards and M. I. Katsnelson, “High-temperature ferromagnetism of *sp* electrons in narrow impurity bands:

- application to CaB_6 ,” *J. Phys.: Condens. Matter* **18**, 7209–7225 (2006).
- ⁵⁵ P. E. Blöchl, “Projector augmented-wave method,” *Phys. Rev. B* **50**, 17953–17979 (1994).
- ⁵⁶ G. Kresse and J. Hafner, “Ab initio molecular dynamics for open-shell transition metals,” *Phys. Rev. B* **48**, 13115 (1993).
- ⁵⁷ G. Kresse and J. Furthmüller, “Efficient iterative schemes for *ab initio* total-energy calculations using a plane-wave basis set,” *Phys. Rev. B* **54**, 11169–11186 (1996).
- ⁵⁸ G. Kresse and D. Joubert, “From ultrasoft pseudopotentials to the projector augmented-wave method,” *Phys. Rev. B* **59**, 1758–1775 (1999).
- ⁵⁹ Th. Böker, R. Severin, A. Müller, C. Janowitz, R. Manzke, D. Voß, P. Krüger, A. Mazur, and J. Pollmann, “Band structure of MoS_2 , MoSe_2 , and $\alpha\text{-MoTe}_2$: Angle-resolved photoelectron spectroscopy and ab initio calculations,” *Phys. Rev. B* **64**, 235305 (2001).
- ⁶⁰ W. C. Jin, P. C. Yeh, N. Zaki, D. T. Zhang, J. T. Sadowski, A. Al-Mahboob, A. M. van der Zande, D. A. Chenet, J. I. Dadap, I. P. Herman, P. Sutter, J. Hone, and R. M. Osgood, “Direct Measurement of the Thickness-Dependent Electronic Band Structure of MoS_2 using Angle-Resolved Photoemission Spectroscopy,” *Phys. Rev. Lett.* **111**, 106801 (2013).
- ⁶¹ J. P. Perdew and A. Zunger, “Self-interaction correction to density-functional approximations for many-electron systems,” *Phys. Rev. B* **23**, 5048–5079 (1981).
- ⁶² John P. Perdew, Kieron Burke, and Matthias Ernzerhof, “Generalized gradient approximation made simple,” *Phys. Rev. Lett.* **77**, 3865–3868 (1996).
- ⁶³ S. T. Pantelides, “The electronic structure of impurities and other point defects in semiconductors,” *Rev. Mod. Phys.* **50**, 797–858 (1978).
- ⁶⁴ M. Lannoo and J. Bourgoin, *Point Defects in Semiconductors I: Theoretical Aspects*, edited by M. Carona, P. Fulde, and H.-J. Queisser, Springer Series in Solid-State Sciences, Vol. 22 (Springer, Berlin, 1981).
- ⁶⁵ M. Altarelli and F. Bassani, “Impurity states: Theoretical,” in *Handbook on Semiconductors edited by T. S. Moss*, Vol. 1, edited by W. Paul (North-Holland, Amsterdam, 1982) pp. 269–322.
- ⁶⁶ J. S. Smith, A. Budi, M. C. Per, N. Vogt, D. W. Drumm, L. C. L. Hollenberg, J. H. Cole, and S. P. Russo, “Ab initio calculation of energy levels for phosphorus donors in silicon,” *Scientific Reports* **7**, 6010 (2017).
- ⁶⁷ O. Gunnarsson, B.I. Lundqvist, and J. W. Wilkins, “Contribution to the cohesive energy of simple metals: Spin-dependent effect,” *Phys. Rev. B* **10**, 1319–1327 (1974).
- ⁶⁸ Martik Aghajanian, Arash A. Mostofi, and Johannes Lischner, “Tuning electronic properties of transition-metal dichalcogenides via defect charge,” *Scientific Reports* **8**, 13611 (2018).
- ⁶⁹ X. L. Yang, S. H. Guo, F. T. Chan, K. W. Wong, and W. Y. Ching, “Analytic solution of a two-dimensional hydrogen atom. I. Nonrelativistic theory,” *Phys. Rev. A* **43**, 1186–1196 (1991).
- ⁷⁰ Akash Laturia, Maarten L. Van de Put, and William G. Vandenberghe, “Dielectric properties of hexagonal boron nitride and transition metal dichalcogenides: from monolayer to bulk,” *npj 2D Materials and Applications* **2**, 6 (2018).
- ⁷¹ W. S. Yun, S. W. Han, S. C. Hong, I. G. Kim, and J. D. Lee, “Thickness and strain effects on electronic structures of transition metal dichalcogenides: 2H-MX₂ semiconductors (M = Mo, W; X = S, Se, Te),” *Phys. Rev. B* **85**, 033305 (2012).
- ⁷² O. Gunnarsson and B.I. Lundqvist, “Exchange and correlation in atoms, molecules, and solids by the spin-density-functional formalism,” *Phys. Rev. B* **13**, 4274–4298 (1976).
- ⁷³ J. F. Janak, “Uniform susceptibilities of metallic elements,” *Phys. Rev. B* **16**, 255–262 (1977).
- ⁷⁴ S. L. Dudarev, G. A. Botton, S. Y. Savrasov, C. J. Humphreys, and A. P. Sutton, “Electron-energy-loss spectra and the structural stability of nickel oxide: An LSDA+U study,” *Phys. Rev. B* **57**, 1505–1509 (1998).
- ⁷⁵ Maokun Wu, Xiaolong Yao, Yuan Hao, Hong Dong, Yahui Cheng, Hui Liu, Feng Lu, Weichao Wang, Kyeongjae Cho, and Wei-Hua Wang, “Electronic structures, magnetic properties and band alignments of 3d transition metal atoms doped monolayer MoS_2 ,” *Phys. Lett. A* **382**, 111–115 (2018).
- ⁷⁶ L. Onsager, “Crystal Statistics. I. A Two-Dimensional Model with an Order-Disorder Transition,” *Phys. Rev.* **65**, 117–149 (1944).
- ⁷⁷ C. N. Yang, “The Spontaneous Magnetization of a Two-Dimensional Ising Model,” *Phys. Rev.* **85**, 808–816 (1952).
- ⁷⁸ A. R. Mackintosh and O. K. Andersen, “The electronic structure of transition metals,” in *Electrons at the Fermi Surface*, edited by M. Springford (Cambridge University Press, Cambridge, 1980) pp. 149–224.
- ⁷⁹ V. Heine, “Electronic structure from the point of view of the local atomic environment,” in *Solid State Physics*, Vol. 35, edited by Henry Ehrenreich, Frederick Seitz, and David Turnbull (Academic Press, New York, 1980) pp. 1–123.
- ⁸⁰ W. Kohn and L. J. Sham, “Self-consistent equations including exchange and correlation effects,” *Phys. Rev.* **140**, A1133–A1138 (1965).
- ⁸¹ G. H. O. Daalderop, P. J. Kelly, and M. F. H. Schuurmans, “First-principles calculation of the magnetocrystalline anisotropy energy of iron, cobalt and nickel,” *Phys. Rev. B* **41**, 11919–11937 (1990).
- ⁸² M. D. Stiles, S. V. Halilov, R. A. Hyman, and A. Zangwill, “Spin-orbit-orbit interaction and magnetocrystalline anisotropy,” *Phys. Rev. B* **64**, 104430 (2001).
- ⁸³ G. H. O. Daalderop, P. J. Kelly, and M. F. H. Schuurmans, “Magnetic anisotropy of a free-standing Co monolayer and of multilayers which contain Co monolayers,” *Phys. Rev. B* **50**, 9989–10003 (1994).
- ⁸⁴ G. H. O. Daalderop, P. J. Kelly, and M. F. H. Schuurmans, “Magnetic anisotropy from first principles,” in *Ultrathin Magnetic Structures I*, edited by J. A. C. Bland and B. Heinrich (Springer-Verlag, Berlin Heidelberg, 1994) pp. 40–64.
- ⁸⁵ Z. Y. Zhu, Y. C. Cheng, and U. Schwingenschlögl, “Giant spin-orbit-induced spin splitting in two-dimensional transition-metal dichalcogenide semiconductors,” *Phys. Rev. B* **84**, 153402 (2011).
- ⁸⁶ The VASP guide, <https://cms.mpi.univie.ac.at/vasp/vasp.pdf>.
- ⁸⁷ G. H. O. Daalderop, P. J. Kelly, and F. J. A. den Broeder, “Prediction and confirmation of perpendicular magnetic anisotropy in Co/Ni multilayers,” *Phys. Rev. Lett.* **68**, 682–685 (1992).
- ⁸⁸ P. E. Blöchl, O. Jepsen, and O. K. Andersen, “Improved tetrahedron method for Brillouin-zone integrations,” *Phys. Rev. B* **49**, 16223–16233 (1994).

- ⁸⁹ Cangsong Xu, Junsheng Feng, Hongjun Xiang, and Laurent Bellaiche, “Interplay between Kitaev interaction and single ion anisotropy in ferromagnetic CrI₃ and CrGeTe₃ monolayers,” *npj Computational Materials* **4**, 57 (2018).
- ⁹⁰ S. A. Leonel, Amanda Castro Oliveira, B. V. Costa, and Pablo Zimmermann Coura, “Comparative study between a two-dimensional anisotropic Heisenberg antiferromagnet with easy-axis single-ion anisotropy and one with easy-axis exchange anisotropy,” *J. Magn. Magn. Mater.* **305**, 157–164 (2006).
- ⁹¹ K. Binder, “Finite size scaling analysis of Ising model block distribution functions,” *Z. Phys. B* **43**, 119–140 (1981).
- ⁹² David P. Landau and Kurt Binder, *A Guide to Monte Carlo Simulations in Statistical Physics*, 3rd ed. (Cambridge University Press, Cambridge, U.K., 2009).
- ⁹³ David Vanderbilt, “Soft self-consistent pseudopotentials in a generalized eigenvalue formalism,” *Phys. Rev. B* **41**, 7892–7895 (1990).
- ⁹⁴ N. Troullier and José Luriaas Martins, “Efficient pseudopotentials for plane-wave calculations,” *Phys. Rev. B* **43**, 1993–2006 (1991).
- ⁹⁵ D. M. Ceperley and B. J. Alder, “Ground state of the electron gas by a stochastic method,” *Phys. Rev. Lett.* **45**, 566–569 (1980).
- ⁹⁶ J. Heyd, G. E. Scuseria, and M. Ernzerhof, “Hybrid functionals based on a screened coulomb potential,” *J. Chem. Phys.* **118**, 8207–8215 (2003); “Erratum: Hybrid functionals based on a screened coulomb potential,” *J. Chem. Phys.* **124**, 219906 (2006).
- ⁹⁷ P. Giannozzi, S. Baroni, N. Bonini, M. Calandra, R. Car, C. Cavazzoni, D. Ceresoli, G. L. Chiarotti, M. Cococcioni, I. Dabo, A. Dal Corso, S. Fabris, G. Fratesi, S. de Gironcoli, R. Gebauer, U. Gerstmann, C. Gougoussis, A. Kokalj, M. Lazzeri, L. Martin-Samos, N. Marzari, F. Mauri, R. Mazzarello, S. Paolini, A. Pasquarello, L. Paulatto, C. Sbraccia, S. Scandolo, G. Sclauzero, A. P. Seitsonen, A. Smogunov, P. Umari, and R. M. Wentzcovitch, “QUANTUM ESPRESSO: a modular and open-source software project for quantum simulations of materials,” *J. Phys.: Condens. Matter* **21**, 395502 (2009).
- ⁹⁸ P. Blaha, K. Schwarz, and G. K. H. Madsen, “Electronic structure calculations of solids using the WIEN2k package for material sciences,” *Comput. Phys. Commun.* **147**, 71–76 (2002).
- ⁹⁹ José M. Soler, Emilio Artacho, Julian D. Gale, Alberto García, Javier Junquera, Pablo Ordejón, and Daniel Sánchez-Portal, “The siesta method for ab initio order-n materials simulation,” *J. Phys.: Condens. Matter* **14**, 2745–2779 (2002).
- ¹⁰⁰ M. Choi, “Strain-enhanced *p* doping in monolayer MoS₂,” *Phys. Rev. Appl.* **9**, 024009 (2018).
- ¹⁰¹ Seok Joon Yun, Dinh Loc Duong, Manh-Ha Doan, Kirandeep Singh, Thanh Luan Phan, Woosoon Choi, Young-Min Kim, and Young Hee Lee, “Room-temperature ferromagnetism in monolayer WSe₂ semiconductor via vanadium dopant,” arXiv:1806.06479.
- ¹⁰² Z. Guguchia, A. Kerelsky, D. Edelberg, S. Banerjee, F. von Rohr, D. Scullion, M. Augustin, M. Scully, D. A. Rhodes, Z. Shermadini, H. Luetkens, A. Shengelaya, C. Baines, E. Morenzoni, A. Amato, J. C. Hone, R. Khasanov, S. J. L. Billinge, E. Santos, A. N. Pasupathy, and Y. J. Uemura, “Magnetism in semiconducting molybdenum dichalcogenides,” *Science Advances* **4**, eeat3672 (2018).
- ¹⁰³ Paula Mariel Coelho, Hannu-Pekka Komsa, Kinga Lasek, Vijaysankar Kalappattil, Jeyakumar Karthikeyan, Manh-Huong Phan, Arkady V. Krasheninnikov, and Matthias Batzill, “Room-temperature ferromagnetism in MoTe₂ by post-growth incorporation of vanadium impurities,” *Advanced Electronic Materials* **5**, 1900044 (2019).
- ¹⁰⁴ Li Yang, Hao Wu, Wenfeng Zhang, Xun Lou, Zijian Xie, Xu Yu, Yuan Liu, and Haixin Chang, “Ta Doping Enhanced Room-Temperature Ferromagnetism in 2D Semiconducting MoTe₂ Nanosheets,” *Advanced Electronic Materials* **5**, 1900552 (2019).
- ¹⁰⁵ M. L. Hu, Zhizhou Yu, K. W. Zhang, L. Z. Sun, and J. X. Zhong, “Synergetic Effect of Substitutional Dopants and Sulfur Vacancy in Modulating the Ferromagnetism of MoS₂ Nanosheets,” *ACS Applied Materials & Interfaces* **11**, 31155–31161 (2019).
- ¹⁰⁶ Yandong Ma, Ying Dai, Meng Guo, Chengwang Niu, Yingtao Zhu, and Baibiao Huang, “Evidence of the existence of magnetism in pristine VX₂ monolayers (X = S, Se) and their strain-induced tunable magnetic properties,” *ACS Nano* **6**, 1695–1701 (2012).
- ¹⁰⁷ C. Ataca, H. Şahin, and S. Ciraci, “Stable, Single-Layer MX₂ Transition-Metal Oxides and Dichalcogenides in a Honeycomb-Like Structure,” *J. Phys. Chem. C* **116**, 8983–8999 (2012).
- ¹⁰⁸ Hui Zhang, Li-Min Liu, and Woon-Ming Lau, “Dimension-dependent phase transition and magnetic properties of VS₂,” *Journal of Materials Chemistry A* **1**, 10821–10828 (2013).
- ¹⁰⁹ Li-Yong Gan, Qingyun Zhang, Yingchun Cheng, and U. Schwingenschlögl, “Two-dimensional ferromagnet/semiconductor transition metal dichalcogenide contacts: *p*-type Schottky barrier and spin-injection control,” *Phys. Rev. B* **88**, 235310 (2013).
- ¹¹⁰ Min Kan, Bo Wang, Young Hee Lee, and Qiang Sun, “A density functional theory study of the tunable structure, magnetism and metal-insulator phase transition in VS₂ monolayers induced by in-plane biaxial strain,” *Nano Research* **8**, 1348–1356 (2015).
- ¹¹¹ A. H. M. Abdul Wasey, Soubhik Chakrabarty, and G. P. Das, “Quantum size effects in layered VX₂ (X=S, Se) materials: Manifestation of metal to semimetal or semiconductor transition,” *J. Appl. Phys.* **117**, 064313 (2015).
- ¹¹² Houlong L. Zhuang and Richard G. Hennig, “Stability and magnetism of strongly correlated single-layer VS₂,” *Phys. Rev. B* **93**, 054429 (2016).